journal

J. Am. Ceram. Soc., 74 [12] 3066–80 (1991)

Steady-State Mechanics of Delamination Cracking in Laminated Ceramic-Matrix Composites

Panos G. Charalambides*

Department of Mechanical Engineering–Engineering Mechanics, Michigan Technological University, Houghton, Michigan 49931

A fracture mechanics delamination cracking model has been developed for brittle-matrix composite laminates. The near-tip mechanics is discussed in the context of material orthotropy and composite material inhomogeneities. A fracture mechanics framework based on the near-tip energy release rate $\mathcal{G}$ and the associated phase angle ψ has been adopted. In the case of steady-state delamination cracking in a prenotched cross-ply symmetric laminated beam, analytical expressions for the steady-state energy release rate, $\mathcal{G}_{ss}$, have been obtained for the combined applied loading of an axial force and a bending moment. Parameter studies assessing the effects on $\mathcal{G}_{ss}$ of load coupling, crack location, and lamination morphology which includes the total number of layers, layer thickness, and material properties are presented. Thus, composite homogenization criteria with respect to the total number of layers placed along the beam height can be obtained for a wide range of material selection. The associated phase angle ψ at the delamination crack tip is discussed in the context of existing solutions. The analysis has been developed based on a theory for structural laminates. The delamination model can be used in conjunction with experimental data obtained from model geometries to extract the mixed-mode transverse composite fracture toughness. Thus, conditions for stable delamination crack growth can be established and design criteria based on toughness for composite laminates and composite fasteners can be obtained. [Key words: cracking, modeling, laminates, composites, mechanics.]

I. Introduction

Ceramic-matrix composites with optimally designed microstructures often exhibit increased resistance to cracks propagating perpendicular to the fiber reinforcements.[1,2] As a consequence, and because of fiber-induced anisotropies, tough ceramic-matrix composites are susceptible to delamination cracking in the presence of notches and manufacturing-drilled holes.[3–7] Typically, when loaded in either tension or bending, cracks initiate near the base of the notch and extend axially[4] (Fig. 1). Such cracking, also evident in polymer-matrix composites[6] and in wood,[7] is often driven by the anisotropy of the composite. This process essentially alleviates the notch sensitivity of the material and may then be regarded as a desirable characteristic of the composite.[3,5] However, experiments indicate that a susceptibility to delamination cracking usually associates with a low transverse fracture resistance and a low interlaminar shear strength. Therefore, the presence and growth of delamination cracks in fiber-reinforced composites and composite laminates may lend to severe reliability and safety problems, such as the reduction of structural stiffness and exposure of the interior to an adverse environment which may cause the final failure. Safe performance of structural composite components then can only be assured through proper understanding of composite toughness and strength in light of the composite fiber-induced anisotropies.

The propagation of "mode I" cracks, i.e., crack plane perpendicular to fiber reinforcements, has been the subject of extensive studies in recent years[1,8–10] and is the subject of many ongoing research programs. Analytical and numerical modeling of composite microstructures, in conjunction with pertinent experimental analysis, provided substantial insights into the effects of microstructure on the mode I mechanical performance of brittle-matrix composite systems. The bridging between the areas of mechanics and materials resulted in a high yield in identifying microstructural failure events such as initial fiber debonding, subsequent debond growth, fiber failure, and frictional fiber pullout and in analyzing how these microstructural failure processes affect the mode I toughness and strength.

In this work, an analogous approach is adopted to study the mechanics of crack propagation for cracks growing *parallel* to the axis of the lamination plane in a cross-ply symmetric brittle-matrix composite laminate. The aim is to develop a refined mechanics framework for the phenomenon of delamination cracking and to invite pertinent experimental work through which transverse composite toughness and strength will be established. This, together with the associated mode I mechanical composite characteristics, will provide the basis for safe and reliable design and use of brittle-matrix composites as structural components.

II. Near-Tip Mechanics

By analogy with fracture in homogeneous systems and with fracture along bimaterial interfaces, delamination cracking in brittle composite systems can be analyzed in the context of near-tip stress singularities. For cracks in homogeneous elastic isotropic systems, the stress and strain fields in the crack tip region are $r^{-1/2}$ singular for all three modes of fracture,[11] i.e., mode I, which causes only a relative opening of the crack surfaces and is also known as the opening mode, mode II or in-plane shearing mode, and mode III or out-of-plane shearing mode. It follows that the stress components at a distance r from the crack tip and an angle Θ measured as shown in Fig. 2 are given in terms of $r^{-1/2}$, a set of universal spatial functions that depend only on Θ and the associated components of the stress intensity factor, K_I for mode I, K_{II} for mode II, and K_{III} for mode III. The latter stress intensities can be obtained by

D. B. Marshall—contributing editor

Manuscript No. 197213. Received October 19, 1990; approved August 12, 1991.

This work was initiated and partially completed while the author was at the Materials Department, University of California, Santa Barbara, CA 93105.

Financial support for this work was provided partially by the Defense Advance Research Project Agency through the University Research Initiative at UCSB under Contract No. N-00014-86-K-0753, by the state of Michigan through the MTU Research Excellence Fund (REF) and by the College of Engineering and ME-EM Department at Michigan Technological University.

*Member, American Ceramic Society.

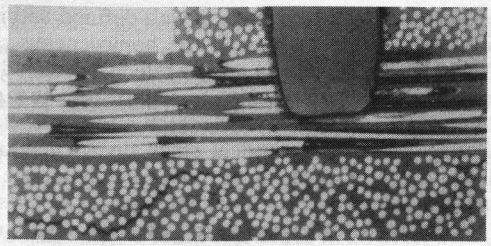

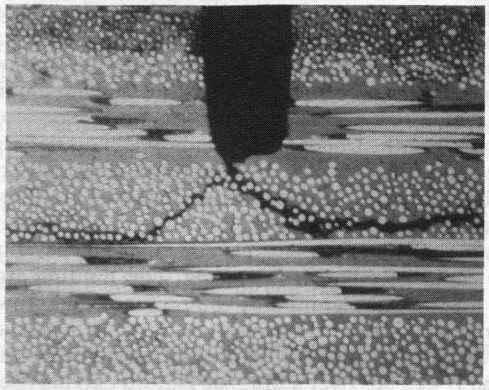

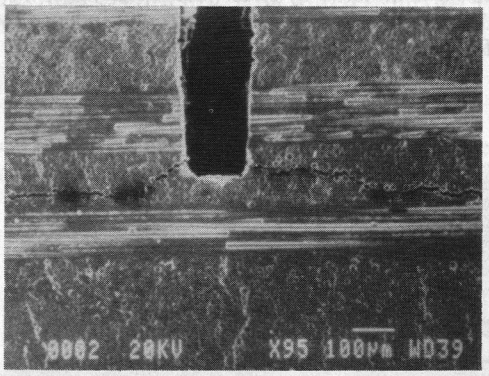

(a)

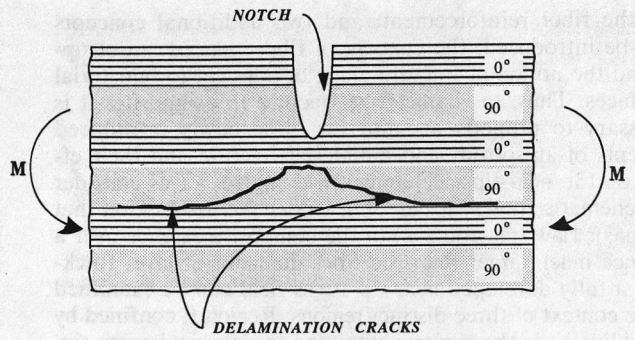

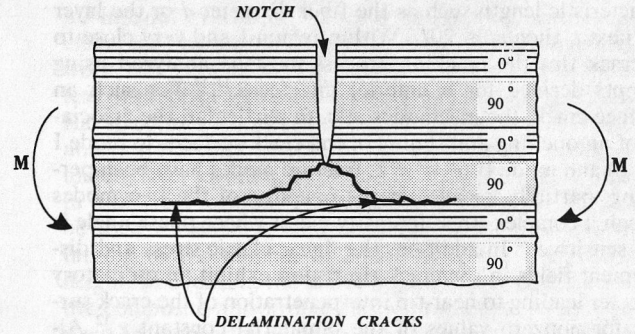

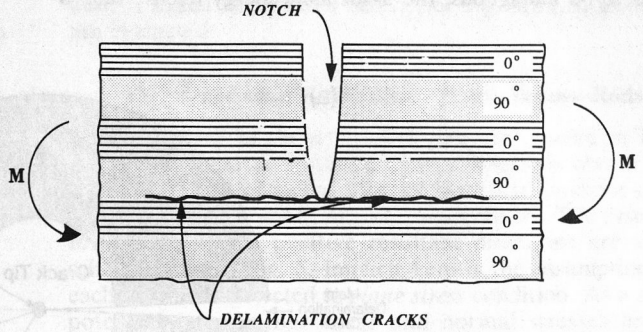

(b)

Fig. 1. (a) Series of optical and scanning electron micrographs which revealed the initial crack trajectory toward the base of the 90° layer as observed by Sbaizero *et al.* in Ref. 4. (b) Schematic of the cracking morphology shown in Fig. 1(a).

and large from the applied loads and from the geometry of the system. Moreover, the nature of the asymptotic solution is such that a nonzero finite energy release rate $\mathcal{G}$ exists at the crack tip and can be obtained from the components of the stress intensity factor and material properties via the generalized Irwin's relationship.[11] In the absence of out-of-plane loading, i.e., $K_{III} = 0$, it is often convenient to represent the tip stress and strain fields in terms of $\mathcal{G}$ and ψ, the energy release rate and the associated phase angle of the complex stress intensity factor $K = K_I + iK_{II} = |K|e^{i\psi}$. The importance of adopting the pair $\mathcal{G}$, ψ as the near-tip characterizing parameters is that $\mathcal{G}$ is a measure of the elastic energy flux to the crack tip due to the application of external loads whereas ψ, defined as $\psi = \arctan(K_{II}/K_I)$, is a measure of the relative in-plane sliding and opening of the crack surfaces. In this last relationship, $|K|$ represents the modulus of the complex K and is uniquely related to $\mathcal{G}$ via the material properties. Thus, in order to fully characterize the stress–strain near-tip fields, one must describe the energy release rate $\mathcal{G}$ and the associated phase angle ψ in terms of the applied loads and geometry of the system. These quantities can then be used to assess crack growth conditions as elaborated later on in this work.

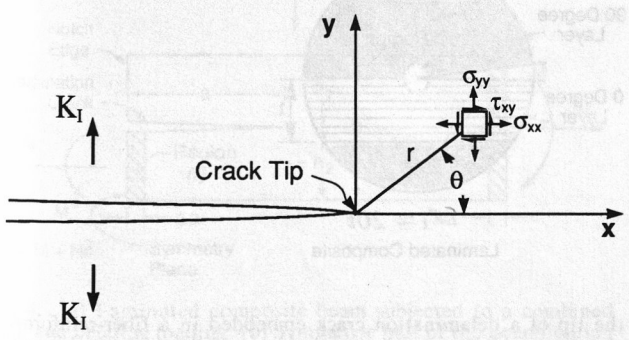

Fig. 2. Near-tip region of a macroscopic crack. Each material point in this region is represented by the polar coordinates r and Θ.

The near-tip mechanics for cracks embedded in composite systems can be analyzed along the same principles discussed for homogeneous systems. However, the nature of the asymptotic near-tip solution in the latter systems is more complex primarily because of the elastic mismatch between the matrix

and the fiber reinforcement, and two additional concepts must be introduced: the concept of fiber-induced anisotropies and the notion of fracture along or adjacent to bimaterial interfaces. Thus, to characterize fracture in composites it is necessary to properly account for these newly introduced concepts of anisotropy and bimaterial fracture and their effects on the near-tip mechanics. In doing so, let us consider the schematic shown in Fig. 3(a). Under the assumption that the major flaw (macrocrack) in the composite extends over a distance much larger than the fiber diameter or layer thickness, a fully developed near-tip stress field can be examined in the context of three distinct regions. Region I, confined by the radius r_1, is the region containing the physical crack tip. The extent of r_1, as shown in Figs. 3(a) and (b), is primarily controlled by the composite microstructure. If L represents a characteristic length such as the fiber diameter d or the layer thickness t, then $r_1 \leq 20L$. Within region I and very close to the crack tip, the cracking process must be analyzed using concepts derived for bimaterial interfaces.[12–17] For such an interface crack, the mechanics and, in particular, the association of an opening and sliding of the crack surfaces to mode I ($\psi = 0$) and mode II ($\psi = \pi/2$) fracture modes have been perplexing, partially because of the coupling of the two modes through a complex stress intensity factor whose phase angle is scale sensitive.[12] In addition, the linear elastic stress and displacement fields in the crack tip region exhibit an oscillatory character leading to near-tip interpenetration of the crack surfaces for nonzero values of the bimaterial constant ε.[12] Although current thinking assumes $\varepsilon = 0$, some of these issues are still the subject of ongoing debate.[12,18,19] On the other hand, and although the definition of the bimaterial phase angle seems to be ambiguous, the associated energy release rate $\mathcal{G}$ at the tip of an interface crack is well-defined and is characterized by the same units as in the homogeneous case (e.g., J/m^2). Moreover, the energy release rate $\mathcal{G}$ calculated from the oscillatory solution is shown to be identical to that predicted by Comninou's contact solution which allows for shear stress singularity only at the physical crack tip.[19] Therefore, in an ideally brittle system, $\mathcal{G}$ can be used to characterize fracture. Ultimately, failure loci of $\mathcal{G}_c$ vs phase angle ψ_c[16,17] should be used to account for the increase in $\mathcal{G}_c$ with ψ_c, as the asperities effects at the bimaterial interface become more important.

However, as shown in Fig. 3(a), region I is embedded within a much larger region II. The mechanics in region I and in particular the energy flux to the crack tip $\mathcal{G}$ are controlled by the stress field in region II, whose dominance extends to a distance r_2 much larger than the composite microstructure. Eventually r_2 would be bounded by the smallest physical specimen dimension such as specimen thickness, specimen height, or crack length. Under these conditions, i.e., $r_2 >> r_1$, small-scale conditions are obtained and thus the presence of region I can be neglected. In this instance, onset of crack growth can be predicted from the mechanics in region II alone. The preceding considerations are general and can be applied to a wide range of composite systems. The limiting argument is that fracture, as signified by the presence and growth of the macrocrack, indeed takes place over a scale much larger than the composite microstructure and thus the dominance of region II extends over a distance $r_2 >> r_1$ giving rise to small-scale near-tip conditions.

On the other hand, the stress and strain fields in region II would be dominated by stress intensities which by and large are driven by the composite anisotropies induced by the fiber reinforcements. These macroscopic anisotropies are expected

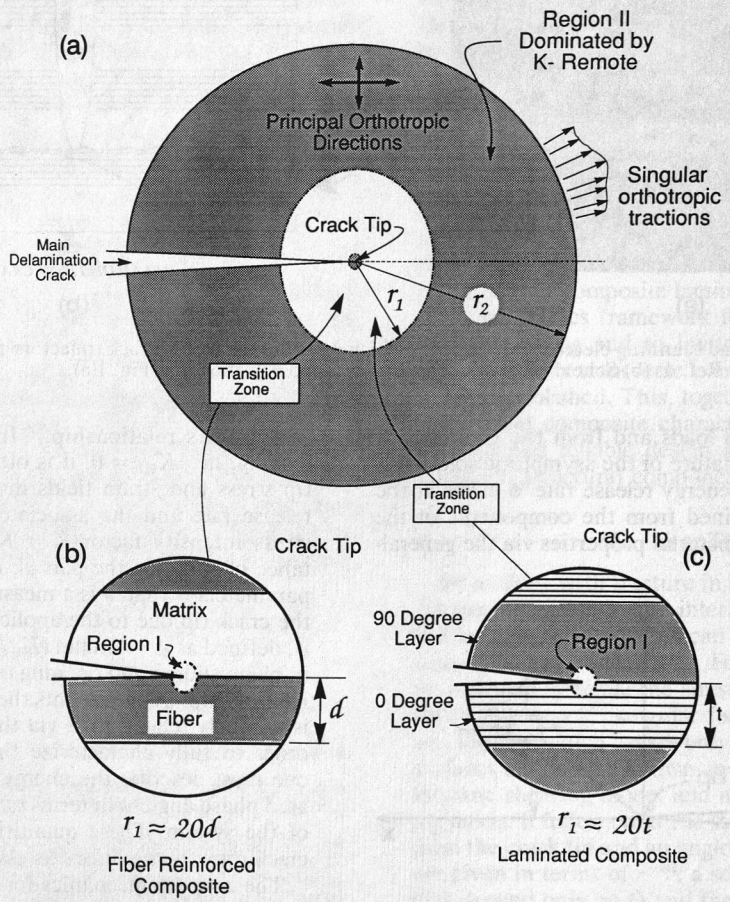

Fig. 3. (a) Schematic representation of small scale conditions near the tip of a delamination crack embedded in a fiber-reinforced or laminated brittle-matrix composite system. The material outside region I is treated as homogeneous orthotropic with its principal directions shown in Fig. 3(a). (b) Crack-tip region embedded in a uniaxially fiber-reinforced composite. (c) Crack-tip region embedded in a laminated fiber-reinforced composite. The regions shown in Figs. 3(b) and (c) are dominated by K_{tip}.

to dominate the mechanics outside region I in a way that composite homogenization techniques can be employed. The objective here is to assume that the material in region II (Fig. 3(a)) is homogeneous orthotropic whose elastic orthotropic properties are obtained in terms of the composite microstructure via composite homogenization procedures. Accordingly, the near-tip mechanics will be derived consistent with the above assumption. Thus, this second asymptotic solution obtained for a crack embedded in an otherwise orthotropic medium would dominate the stress–strain fields in region II via an orthotropic stress intensity factor. Other nonsingular terms are expected to dominate in the solutions for the stresses and strains in the domain beyond region II. A summary of the constitutive relations and the near-tip mechanics in an orthotropic material is presented in Appendix A. In this article, the intent is to assume region II as a region of dominance and thus make use of the mechanics summarized in Appendix A. The objective is to establish the mechanics framework within which delamination cracking in composites can be studied. Thus, analysis of the cracking process will be predicted through relationships between the tip energy release rate $\mathcal{G}$, the phase angle of loading ψ, the crack length a, and the loading within an elastically orthotropic body.

III. Steady-State Delamination Energy Release Rates

In a linear elastic system the energy release rate $\mathcal{G}$ can be obtained in terms of the changes in either the total potential energy Ψ or the total strain energy U of the system as the crack grows from length a to $a + \Delta a$ with Δ signifying a small increment of the quantity following it, i.e.,

$$\mathcal{G} = -\left(\frac{\partial \Psi}{\partial a}\right)_{\text{Constant Loads}} = \left(\frac{\partial U}{\partial a}\right)_{\text{Constant Loads}} \tag{1}$$

For a linear elastic system, $\Psi = -U$. The steady-state delamination energy release rate for the geometry shown in Fig. 4(a) can now be derived from the changes in U as the crack grows from a to $a + \Delta a$, i.e.,

$$\mathcal{G}_{ss} = \left(\frac{U(a + \Delta a) - U(a)}{\Delta a}\right)_{\text{Constant Loads}} \tag{2}$$

A schematic of virtual crack extension is shown in Fig. 4(b). With the aid of this figure, the delamination steady-state energy release rate can be readily estimated as the difference in the strain energies in a strip of composite laminated beam of length Δa far behind and far ahead of the crack tip,[14,15] i.e.,

$$\mathcal{G}_{ss} = \left(\frac{U_i - U_{ii}}{\Delta a}\right)_{\text{Constant Loads}} \tag{3}$$

The expression for $\mathcal{G}_{ss}$ given by Eq. (3) can also be derived via a J-integral evaluation,[11] over a remote perimeter contour as elaborated elsewhere.[20] For the purpose of the analyses in this work, the required solutions for U will be obtained in the context of theories applied to bending and stretching of laminated flat structures composed of orthotropic lamina. Through such analysis, the effects on $\mathcal{G}_{ss}$ of the crack location, material mismatch, layer location, and relative layer size will be addressed in a discreet fashion. The resulting solution for $\mathcal{G}_{ss}$ will then be used to establish composite homogenization criteria pertaining to the number of layers along the composite beam height. In addition, the above approach will yield formulas for the composite anisotropic elastic properties ρ and Λ summarized in Appendix A. Such solutions will be sought for the more general case of an applied moment coupled with an applied axial force. We shall now present elements of the laminated theory in the context of which the strain energies U_i and U_{ii} stored in regions i and ii (see Fig. 4(b)), respectively, are evaluated.

IV. Laminated Composites: Plates–Beams–Rods

The solution to the composite geometry shown in Fig. 4 will be obtained as a special case of solutions obtain for a laminated plate subjected to axial force and moment resultants N_x, N_y, N_{xy} and M_x, M_y, M_{xy}, respectively. The system of reference and the positive resultant directions are shown schematically in Fig. 5. Implicit here is the assumption that each lamina is subjected to *plane stress* condition. As a result, potential interlaminar shear and normal stresses are neglected in the analysis, and thus the stress resultants N_z, N_{xz}, N_{yz} are taken to be zero. In addition, the shear stress components τ_{xz}, τ_{yz} due to a nonzero torque, i.e., $M_{xy} \neq 0$, are neglected as being much smaller compared to other stress components. Under the above assumptions, the stress–strain relations within each randomly oriented orthotropic lamina can be found in Appendix A expressed via Eqs. (A–7), (A–8),

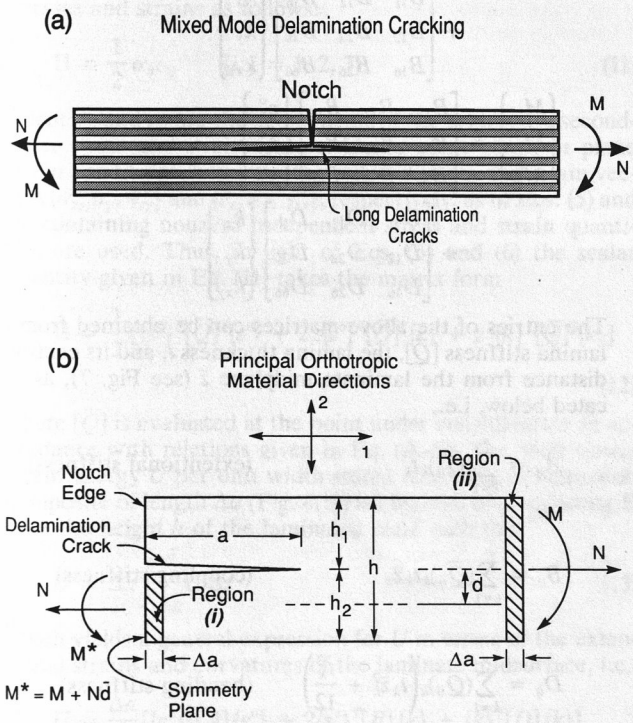

Fig. 4. (a) Laminated composite beam subjected to a combined axial and bending loading. (b) Symmetric half of the delamination geometry shown in Fig. 4(a). Solutions for the elastic strain energy in regions i and ii are used to evaluate the elastic energy release rate at the tip of the delamination crack tip.

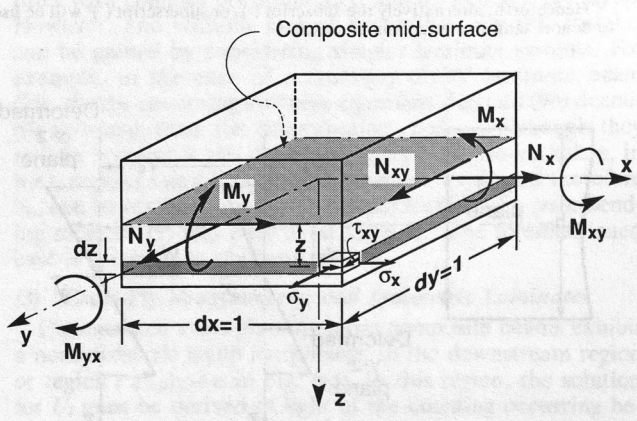

Fig. 5. Unit cell used in developing the self-consistent theory for laminate plates. The load and moment resultants shown are assumed to be positive.

and (A–9). For a ply oriented along its principal orthotropic axes, the stress–strain relations reduce to those given by Eqs. (A–5) and (A–6) in Appendix A. The theory of laminated structures can be found elsewhere.[21,22] In the following section we shall summarize the basic steps in obtaining composite elastic solutions under the above assumptions when the laminated plate is subjected to the general loading schematically shown in Fig. 5.

(1) Deformation Hypothesis

Assuming that plane sections remain plane after deformation, the displacement field is obtained with the aid of Fig. 6,[21,22] i.e.,

$$u(x, y, z) = u^{\circ}(x, y) + z\frac{\partial w^{\circ}(x,y)}{\partial x} \tag{4a}$$

$$v(x, y, z) = v^{\circ}(x, y) + z\frac{\partial w^{\circ}(x,y)}{\partial y} \tag{4b}$$

$$w(x, y, z) = w^{\circ}(x, y) \tag{4c}$$

where u°,[†] v°, and w° are the displacement components of the laminate midplane. Also, z in the above relations denotes the distance of a given material point from the laminate midplane as shown in Figs. 6 and 7. Thus, the following strain field obtains:

$$\begin{Bmatrix}\varepsilon_x\\ \varepsilon_y\\ \gamma_{xy}\end{Bmatrix} = \begin{Bmatrix}\varepsilon_x^{\circ}\\ \varepsilon_y^{\circ}\\ \gamma_{xy}^{\circ}\end{Bmatrix} + z\begin{Bmatrix}k_x\\ k_y\\ k_{xy}\end{Bmatrix} \tag{5}$$

where $k_x = \partial^2 w^{\circ}/\partial^2 x$, $k_y = \partial^2 w^{\circ}/\partial^2 y$, and $k_{xy} = \partial^2 w^{\circ}/(\partial x\ \partial y)$ are the curvatures of the deformed plate in the x–z, y–z, and x–y planes.[21,22] With the aid of Eqs. (A–8) in Appendix A, the stress field within the kth lamina (see Fig. 7) is given by

$$\begin{Bmatrix}\sigma_x\\ \sigma_y\\ \tau_{xy}\end{Bmatrix} = \begin{bmatrix}\bar{Q}_{11} & \bar{Q}_{12} & \bar{Q}_{16}\\ \bar{Q}_{12} & \bar{Q}_{22} & \bar{Q}_{26}\\ \bar{Q}_{16} & \bar{Q}_{26} & \bar{Q}_{66}\end{bmatrix}\begin{Bmatrix}\varepsilon_x^{\circ}\\ \varepsilon_y^{\circ}\\ \gamma_{xy}^{\circ}\end{Bmatrix} + z\begin{bmatrix}\bar{Q}_{11} & \bar{Q}_{12} & \bar{Q}_{16}\\ \bar{Q}_{12} & \bar{Q}_{22} & \bar{Q}_{26}\\ \bar{Q}_{16} & \bar{Q}_{26} & \bar{Q}_{66}\end{bmatrix}\begin{Bmatrix}k_x\\ k_y\\ k_{xy}\end{Bmatrix} \tag{6}$$

In accordance with the schematic of Fig. 5, the stress resultants per unit width are obtained by integrating over the laminate height as follows:

$$\begin{Bmatrix}N_x\\ N_y\\ N_{xy}\end{Bmatrix} = \int_{-h/2}^{h/2}\begin{Bmatrix}\sigma_x\\ \sigma_y\\ \tau_{xy}\end{Bmatrix} dz \tag{7a}$$

[†]Henceforth, alternatively the subscript ( )$_0$ or superscript ( )$^{\circ}$ will be used to denote laminate midplane quantities.

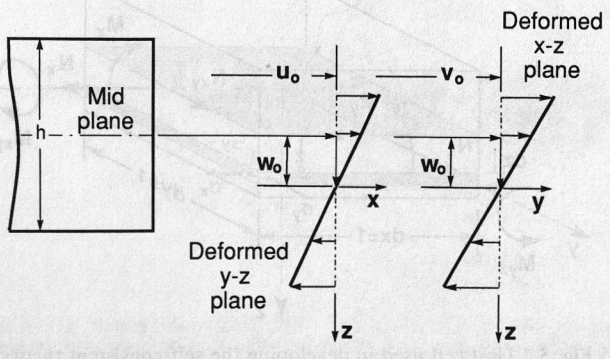

Fig. 6. Deformation hypothesis is based on cross-sectional planarity after deformation as shown schematically above.

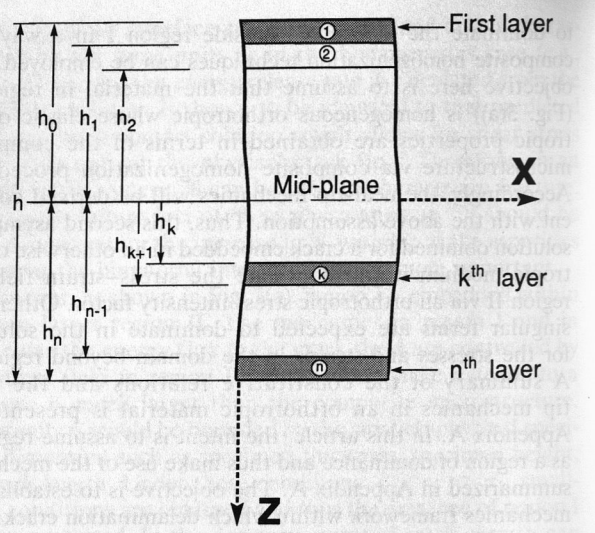

Fig. 7. Schematic indicating characteristics of the lamination morphology in a composite laminate.

$$\begin{Bmatrix}M_x\\ M_y\\ M_{xy}\end{Bmatrix} = \int_{-h/2}^{h/2}\begin{Bmatrix}\sigma_x\\ \sigma_y\\ \tau_{xy}\end{Bmatrix} z\ dz \tag{7b}$$

Assuming constant material properties within each lamina, the above relations take the indicial form

$$N_i = A_{ij}\varepsilon_j^{\circ} + B_{ij}k_j \qquad (i, j = 1, 2, 6) \tag{8a}$$

$$M_i = B_{ij}\varepsilon_j^{\circ} + D_{ij}k_j \qquad (i, j = 1, 2, 6) \tag{8b}$$

Using matrix notation, the above formulas become

$$\begin{Bmatrix}N_x\\ N_y\\ N_{xy}\end{Bmatrix} = \begin{bmatrix}A_{11} & A_{12} & A_{16}\\ A_{12} & A_{22} & A_{26}\\ A_{16} & A_{26} & A_{66}\end{bmatrix}\begin{Bmatrix}\varepsilon_x^{\circ}\\ \varepsilon_y^{\circ}\\ \gamma_{xy}^{\circ}\end{Bmatrix} + \begin{bmatrix}B_{11} & B_{12} & B_{16}\\ B_{12} & B_{22} & B_{26}\\ B_{16} & B_{26} & B_{66}\end{bmatrix}\begin{Bmatrix}k_x\\ k_y\\ k_{xy}\end{Bmatrix} \tag{9a}$$

$$\begin{Bmatrix}M_x\\ M_y\\ M_{xy}\end{Bmatrix} = \begin{bmatrix}B_{11} & B_{12} & B_{16}\\ B_{12} & B_{22} & B_{26}\\ B_{16} & B_{26} & B_{66}\end{bmatrix}\begin{Bmatrix}\varepsilon_x^{\circ}\\ \varepsilon_y^{\circ}\\ \gamma_{xy}^{\circ}\end{Bmatrix} + \begin{bmatrix}D_{11} & D_{12} & D_{16}\\ D_{12} & D_{22} & D_{26}\\ D_{16} & D_{26} & D_{66}\end{bmatrix}\begin{Bmatrix}k_x\\ k_y\\ k_{xy}\end{Bmatrix} \tag{9b}$$

The entries of the above matrices can be obtained from the lamina stiffness $[\bar{Q}]$, the lamina thickness t, and its centroidal distance from the laminate midplane $\bar{z}$ (see Fig. 7), as indicated below, i.e.,

$$A_{ij} = \sum_{k=1}^{n}(\bar{Q}_{ij})_k t_k \qquad \text{(extentional stiffness)} \tag{10a}$$

$$B_{ij} = \sum_{k=1}^{n}(\bar{Q}_{ij})_k t_k \bar{z}_k \qquad \text{(coupling stiffness)} \tag{10b}$$

$$D_{ij} = \sum_{k=1}^{n}(\bar{Q}_{ij})_k\left(t_k\bar{z}_k^2 + \frac{t_k^3}{12}\right) \qquad \text{(bending stiffness)} \tag{10c}$$

(2) Elastic Strain Energy

The elastic strain energy density is a pointwise defined quantity and for a linear system is given in terms of the

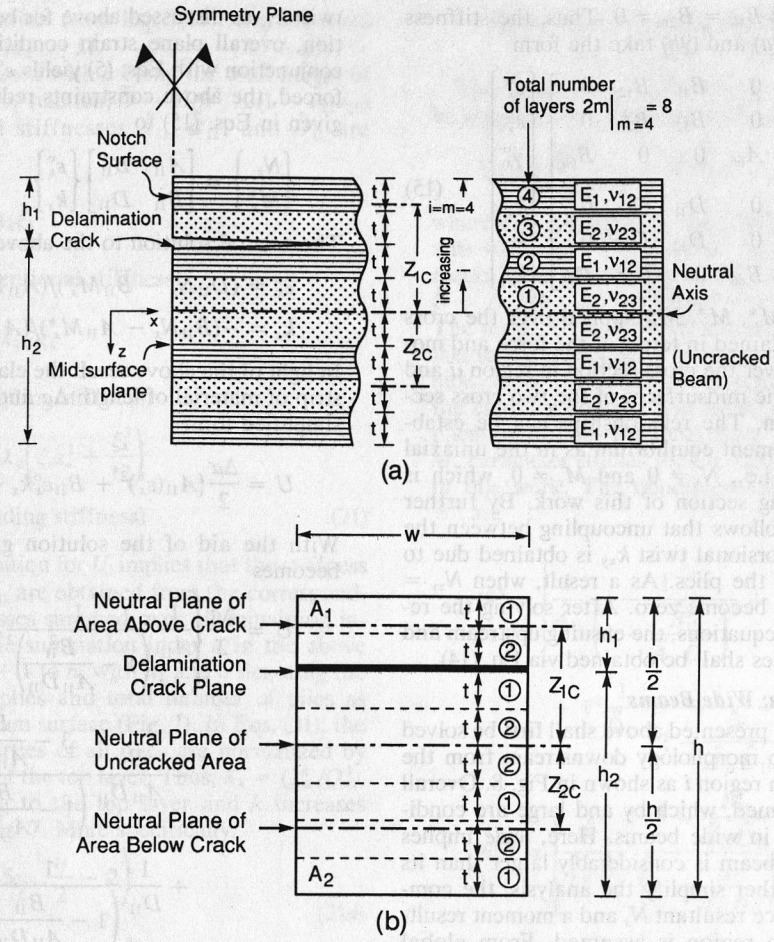

Fig. 8. (a) Schematic of the symmetric half of a prenotched symmetric laminated beam subject to delamination cracking at the base of the notch. (b) Cross section of the notch location of the system shown in Fig. 8(a).

stresses and strains as follows:

$$\Pi = \frac{1}{2}\sigma_{ij}\varepsilon_{ij} \qquad (i, j = 1, 2, 3) \tag{11}$$

where σ_{ij} and ε_{ij} are the components of the symmetric second-order stress and strain tensors. Under plane stress or plane strain conditions, however, the reduced stress and strain vectors $\{\sigma_x, \sigma_y, \tau_{xy}\}$ and $\{\varepsilon_x, \varepsilon_y, \gamma_{xy}\}$, respectively, as in Eqs. (5) and (6) containing nonzero independent stress and strain quantities are used. Thus, in light of Eqs. (5) and (6) the scalar quantity given in Eq. (11) takes the matrix form

$$\Pi = \frac{1}{2}[\{\varepsilon^\circ\}^T[\bar{Q}]^T\{\varepsilon^\circ\} + 2z\{\varepsilon^\circ\}^T[\bar{Q}]^T\{k\} + z^2\{k\}^T[\bar{Q}]^T\{k\}] \tag{12}$$

where $[\bar{Q}]$ is evaluated at the point under consideration in accordance with relations given in Eq. (A–9). The total elastic strain energy U per unit width stored in a strip of laminated composite of length Δa (Fig. 4(b)) is obtained by integrating Π over the height h of the laminated plate such that

$$U = \Delta a \int_{-h/2}^{h/2} \Pi \, dz \tag{13}$$

which yields a general expression for U in terms of the extensional strains and curvatures of the laminate midsurface, i.e.,

$$U = \frac{\Delta a}{2}[\{\varepsilon^\circ\}^T[A]\{\varepsilon^\circ\} + 2\{\varepsilon^\circ\}^T[B]\{k\} + \{k\}^T[D]\{k\}] \tag{14}$$

The central theme of this work is the evaluation of the steady-state energy release rate at the delamination crack tip of the model laminate geometry shown in Fig. 4(a). The results will be obtained with the aid of Eq. (3) wherein values for U far *upstream* (region *ii*) and far *downstream* (region *i*) from the crack tip are required. For a prescribed set of applied loads and boundary conditions, general *numerical* solutions for $\mathcal{G}_{ss}$ can be obtained for arbitrary lamination morphologies. Typically, the axial strains ε_x°, ε_y°, γ_{xy}°, and midsurface curvatures k_x, k_y, k_{xy} are first obtained in terms of the applied loads by solving numerically the coupled system of equations described in Eqs. (9*a*) and (9*b*). Subsequently, Eq. (14) is used to evaluate U in regions *i* and *ii*. The corresponding energy release rate can then be obtained via Eq. (3). Such analysis can be fairly involved, especially in the case of laminate structures with complex ply orientation and asymmetric ply layup. However, and without loss of generality, physical insights can be gained by considering simpler laminate systems. For example, in the case of a cross-ply 0°/90° laminate beam (Fig. 8), the governing stiffness equations (9*a*) and (9*b*) decouple upstream from the delamination crack tip although they remain coupled in the downstream solution. Nevertheless, in both regions *i* and *ii* analytical solutions for U and therefore $\mathcal{G}_{ss}$ can be obtained for the combined loading of a pure bending moment M_x and pure axial force N_x. The foremention case is taken on in the next section.

(3) Cross-Ply Nonsymmetric and Symmetric Laminates

Delaminated cross-ply symmetric composite beams exhibit a nonsymmetric layup morphology in the downstream region or region *i* as shown in Fig. 8(a). In this region, the solution for U_i must be derived in light of the coupling occurring between axial and bending loadings via the nonzero coupling matrix $[B]$. In particular, the 0°/90° directionality of the plies through Eqs. (A–6) to (A–9) and (10) implies that $A_{16} = A_{26} =$

$D_{16} = D_{26} = 0$ as well as $B_{16} = B_{26} = 0$. Thus, the stiffness relations given by Eqs. (9*a*) and (9*b*) take the form

$$\begin{Bmatrix} N_x \\ N_y \\ N_{xy} \\ M_x^* \\ M_y^* \\ M_{xy}^* \end{Bmatrix} = \begin{bmatrix} A_{11} & A_{12} & 0 & B_{11} & B_{12} & 0 \\ A_{12} & A_{22} & 0 & B_{12} & B_{22} & 0 \\ 0 & 0 & A_{66} & 0 & 0 & B_{66} \\ B_{11} & B_{12} & 0 & D_{11} & D_{12} & 0 \\ B_{12} & B_{22} & 0 & D_{12} & D_{22} & 0 \\ 0 & 0 & B_{66} & 0 & 0 & D_{66} \end{bmatrix} \begin{Bmatrix} \varepsilon_x^\circ \\ \varepsilon_y^\circ \\ \gamma_{xy}^\circ \\ k_x \\ k_y \\ k_{xy} \end{Bmatrix} \tag{15}$$

The moment resultants M_x^*, M_y^*, M_{xy}^* applied over the cross section in region *i* are obtained in terms of the force and moment resultants applied over the cross section in region *ii* and the distance $\bar{d}$ between the midsurfaces of the two cross sections under consideration. The relationships can be established through global moment equilibrium as in the uniaxial combined loading case, i.e., $N_x \neq 0$ and $M_x \neq 0$, which is taken on in the following section of this work. By further examining Eqs. (15), it follows that uncoupling between the axial shear γ_{xy}° and the torsional twist k_{xy} is obtained due to the 0°/90° orientation of the plies. As a result, when $N_{xy} = M_{xy}^* = 0$ both γ_{xy}° and k_{xy} become zero. After solving the remaining 4 × 4 system of equations, the ensuing upstream and downstream strain energies shall be obtained via Eq. (14).

(4) Overall Plane Strain; Wide Beams

The system of Eqs. (15) presented above shall first be solved for the asymmetric layup morphology downstream from the delamination crack tip, in region *i* as shown in Fig. 8. Overall plane strain will be assumed, which by and large are conditions often encountered in wide beams. Here, *wide* implies that the width *w* of the beam is considerably larger than its height *h* (Fig. 9). To further simplify the analysis, the combined application of a force resultant N_x and a moment resultant M_x in the upstream region is assumed. From global equilibrium their resultant force and moment counterparts applied in the downstream region are N_x and $M_x^* = M_x - \bar{d}N_x$, respectively, which are transmitted through region *i* as shown in Fig. 4(b). This type of loading due to the 0°/90° ply orientation (see Fig. 8) gives rise to zero axial shear γ_{xy}° and torsional twist k_{xy} as discussed above for both regions *i* and *ii*. In addition, overall plane strain condition implies $\varepsilon_y = 0$. This in conjunction with Eqs. (5) yields $\varepsilon_y^\circ = 0$ and $k_y = 0$. When enforced, the above constraints reduce the system of equations given in Eqs. (15) to

$$\begin{Bmatrix} N_x \\ M_x^* \end{Bmatrix} = \begin{bmatrix} A_{11} & B_{11} \\ B_{11} & D_{11} \end{bmatrix} \begin{Bmatrix} \varepsilon_x^\circ \\ k_x \end{Bmatrix} \tag{16}$$

The general solution to the above system is

$$\varepsilon_x^\circ = (D_{11}N_x - B_{11}M_x^*)/(A_{11}D_{11} - B_{11}^2) \tag{17a}$$

$$k_x = -(B_{11}N_x - A_{11}M_x^*)/(A_{11}D_{11} - B_{11}^2) \tag{17b}$$

In light of the above result the elastic strain energy stored in a strip of material of length Δa and given by Eq. (14) takes the simplified form

$$U = \frac{\Delta a}{2}\{A_{11}(\varepsilon_x^\circ)^2 + B_{11}\varepsilon_x^\circ k_x + D_{11}(k_x)^2\} \tag{18}$$

With the aid of the solution given in Eqs. (17), Eq. (18) becomes

$$U = \frac{\Delta a}{2}\left\{\frac{1}{A_{11}}\frac{1}{\left(1 - \dfrac{B_{11}^2}{A_{11}D_{11}}\right)^2}N_x^2 - \frac{B_{11}}{A_{11}D_{11}}\frac{3 - \dfrac{B_{11}^2}{A_{11}D_{11}}}{\left(1 - \dfrac{B_{11}^2}{A_{11}D_{11}}\right)^2}N_x M_x^* + \frac{1}{D_{11}}\frac{1}{\left(1 - \dfrac{B_{11}^2}{A_{11}D_{11}}\right)^2}(M_x^*)^2\right\} \tag{19}$$

The latter expression for *U* can now be used to estimate the strain energy stored in strips of the composite laminate in both the downstream and upstream regions. In particular the solution for *U* in region *i* takes the form

$$U_i = \frac{\Delta a M^2}{24\bar{D}}\left\{\left[\frac{1}{\hat{A}_{11}}\frac{1}{\left(1 - \dfrac{\hat{B}_{11}^2}{\hat{A}_{11}\hat{D}_{11}}\right)^2} + \bar{y}\frac{\hat{B}_{11}}{\hat{A}_{11}\hat{D}_{11}}\frac{3 - \dfrac{\hat{B}_{11}^2}{\hat{A}_{11}\hat{D}_{11}}}{\left(1 - \dfrac{\hat{B}_{11}^2}{\hat{A}_{11}\hat{D}_{11}}\right)^2} + \bar{y}^2\frac{1}{\hat{D}_{11}}\frac{1}{\left(1 - \dfrac{\hat{B}_{11}^2}{\hat{A}_{11}\hat{D}_{11}}\right)^2}\right]_i\left(\frac{hN}{M}\right)^2 + \left[\frac{\hat{B}_{11}}{\hat{A}_{11}\hat{D}_{11}}\frac{3 - \dfrac{\hat{B}_{11}^2}{\hat{A}_{11}\hat{D}_{11}}}{\left(1 - \dfrac{\hat{B}_{11}^2}{\hat{A}_{11}\hat{D}_{11}}\right)^2} + 2\bar{y}\frac{1}{\hat{D}_{11}}\frac{1}{\left(1 - \dfrac{\hat{B}_{11}^2}{\hat{A}_{11}\hat{D}_{11}}\right)^2}\right]_i\left(\frac{hN}{M}\right) + \left[\frac{1}{\hat{D}_{11}}\frac{1}{\left(1 - \dfrac{\hat{B}_{11}^2}{\hat{A}_{11}\hat{D}_{11}}\right)^2}\right]_i\right\} \tag{20}$$

which relation is now expressed in terms of the applied axial load *N* and bending moment *M* consistent with Fig. 4(b). In

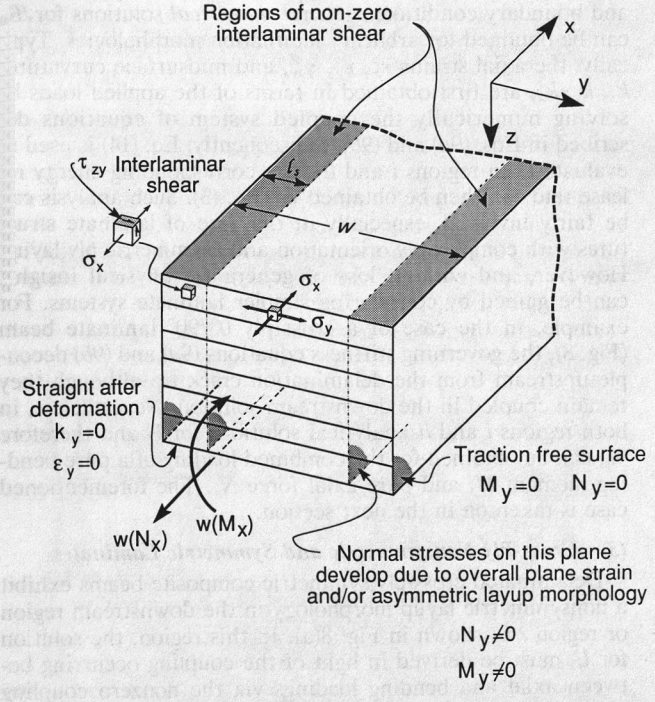

Fig. 9. Schematic illustrating regions of interlaminar shear in a composite laminate.

deriving the above equation from Eqs. (19), the relations $M_x = -M$, $N_x = N$, and $M_x^* = M_x - \bar{d}N_x = -(M + \bar{d}N) = -M^*$ with $\bar{d} = \bar{y}h$ were used with h being the total height of the beam. Also in the above relation, $\bar{D} = E_1 h^3/12(1 - \nu_{12}\nu_{21})$ whereas the normalized stiffnesses $\hat{A}_{11}$, $\hat{B}_{11}$, and $\hat{D}_{11}$ are given by

$$\hat{A}_{11} = \frac{A_{11}}{Q_{11}h} = \sum_{k=n_1+1}^{n} \lambda_k \xi_k$$

(normalized extentional stiffness)

$$\hat{B}_{11} = \frac{B_{11}}{Q_{11}h^2} = \sum_{k=n_1+1}^{n} \lambda_k \xi_k \hat{\bar{z}}_k$$

(normalized coupling stiffness)

$$\hat{D}_{11} = \frac{D_{11}}{Q_{11}h^3} = \sum_{k=n_1+1}^{n} \lambda_k \left(\xi_k \hat{\bar{z}}_k^2 + \frac{\xi_k^3}{12} \right)$$

(normalized bending stiffness) (21)

The subscript i in the equation for U_i implies that the stiffness constants $\hat{A}_{11}$, $\hat{B}_{11}$, and $\hat{D}_{11}$ are obtained from the corresponding individual ply stiffnesses summed over all remaining intact plies. As a result, the summation index k in the above equations varies from $n_1 + 1$ to n, with n_1 and n denoting the number of delaminated plies and total number of plies as measured from the top beam surface (Fig. 7). In Eqs. (21), the longitudinal elastic properties of all plies are normalized by the respective properties of the top layer. Thus, $\lambda_k = Q_{xx}^k/Q_{xx}^1$, with $k = 1$ corresponding to the top layer and k increases downward as shown in Fig. 7. More specifically,

$$\lambda_k = \begin{cases} 1 & \left(k = 1, 3, 5, \ldots \frac{n}{2} - 2\right) \\ \frac{E_2}{E_1} & (k = 2, 4, 6, \ldots, n-1) \end{cases} \tag{21a}$$

$$\lambda_k = \begin{cases} 1 & \left(k = \frac{n}{2} + 2, \frac{n}{2} + 4, \ldots, n\right) \\ \frac{E_2}{E_1} & \left(k = \frac{n}{2} + 1, \frac{n}{2} + 3, \ldots, n-1\right) \end{cases} \tag{21b}$$

Also in Eqs. (21), $\xi_k = t_k/h$ is the normalized layer thickness and $\hat{\bar{z}} = \bar{z}/h$ is the normalized layer centroidal distance from the composite midsurface. A more simplified form for U obtains in the symmetric or upstream region of the specimen geometry shown in Fig. 8. For this section, the coupling stiffness matrix $[B]$ is identical to zero, i.e., $B_{ij} = 0$, $i, j = 1, 2, 6$, and thus Eq. (19) further reduces to

$$U_{ii} = \frac{\Delta a M^2}{24\bar{D}} \left\{ \frac{1}{\hat{A}_{11}} \left(\frac{hN_x}{M_x} \right)^2 + \frac{1}{\hat{D}_{11}} \right\}_{ii} \tag{22}$$

In the latter equation, the normalized stiffnesses $\hat{A}_{11}$ and $\hat{D}_{11}$ can be obtained with the aid of Eqs. (21) but with the summation index k now varying from 1 to n. The above expressions for U_i and U_{ii} given by Eqs. (20) and (22) account for the presence of normal stresses within the laminated strip and do not incorporate interlaminar shear stress contributions. For example, overall plane strain conditions, i.e., $\varepsilon_y^\circ = 0$ and $k_y = 0$, give rise to nonzero out-of-plane axial force N_y and moment M_y and M_y^* via Eqs. (15). Thus, a biaxial stress state obtains within the inner region of the laminated beam as shown schematically in Fig. 9. However, traction-free conditions exist on the outer lateral surfaces of the beam. Thus, a region of interlaminar shear, in this case τ_{zy}, develops close to the lateral surfaces and extends inward to a distance l_s as shown in Fig. 9. The assumption in this analysis is that the interlaminar shear strain energy contribution is much smaller compared to that due to normal stresses as expressed by Eqs. (20) and (22).

V. Delamination Energy Release Rate; Applied Moment and Axial Force

The steady-state delamination energy release rate, $\mathcal{G}_{ss}$, can be obtained by combining Eqs. (3), (20), and (22) such that

$$\mathcal{G}_{ss} \frac{24\bar{D}}{S^2 h^2 \cos^2 \phi} = \mathcal{G}^N \tan^2 \phi + \mathcal{G}^{NM} \tan \phi + \mathcal{G}^M \tag{23}$$

where ϕ is a measure of the relative force and moment resultants such that $N = S \sin \phi$, $M = Sh \cos \phi$ as shown schematically in the sketch of Fig. 10. In addition, in Eq. (23), $\bar{D} = E_1 I/(1 - \nu_{12}\nu_{21})$ with $I = h^3/12$ and h the beam height. The terms $\mathcal{G}^N$ and $\mathcal{G}^M$ are the individual contributions to $\mathcal{G}_{ss}$ due to the independent presence of the axial force N and the moment M, respectively. The term $\mathcal{G}^{NM} \sin \phi \cos \phi$ represents the coupling contribution to $\mathcal{G}_{ss}$ during the simultaneous application of both the axial force N and the bending moment M. Parameter studies for Eq. (23) will be undertaken later on in this work. The nondimensional functions $\mathcal{G}^N$, $\mathcal{G}^{NM}$, and $\mathcal{G}^M$ are

$$\mathcal{G}^N = \left[\frac{1}{\hat{A}_{11}} \frac{1}{\left(1 - \frac{\hat{B}_{11}^2}{\hat{A}_{11}\hat{D}_{11}}\right)^2} + \bar{y} \frac{\hat{B}_{11}}{\hat{A}_{11}\hat{D}_{11}} \frac{3 - \frac{\hat{B}_{11}^2}{\hat{A}_{11}\hat{D}_{11}}}{\left(1 - \frac{\hat{B}_{11}^2}{\hat{A}_{11}\hat{D}_{11}}\right)^2} + \bar{y}^2 \frac{1}{\hat{D}_{11}} \frac{1}{\left(1 - \frac{\hat{B}_{11}^2}{\hat{A}_{11}\hat{D}_{11}}\right)^2} \right]_i - \left[\frac{1}{\hat{A}_{11}} \right]_{ii} \tag{24a}$$

$$\mathcal{G}^{NM} = \left[\frac{\hat{B}_{11}}{\hat{A}_{11}\hat{D}_{11}} \frac{3 - \frac{\hat{B}_{11}^2}{\hat{A}_{11}\hat{D}_{11}}}{\left(1 - \frac{\hat{B}_{11}^2}{\hat{A}_{11}\hat{D}_{11}}\right)^2} + 2\bar{y} \frac{1}{\hat{D}_{11}} \frac{1}{\left(1 - \frac{\hat{B}_{11}^2}{\hat{A}_{11}\hat{D}_{11}}\right)^2} \right]_i \tag{24b}$$

$$\mathcal{G}^M = \left[\frac{1}{\hat{D}_{11}} \frac{1}{\left(1 - \frac{\hat{B}_{11}^2}{\hat{A}_{11}\hat{D}_{11}}\right)^2} \right]_i - \left[\frac{1}{\hat{D}_{11}} \right]_{ii} \tag{24c}$$

VI. Composite Laminate Stiffnesses

In this section the normalized laminate stiffnesses $\hat{A}_{11}$, $\hat{B}_{11}$, and D_{11} given by Eqs. (21) will be determined in terms of the cross-sectional morphology of the composite laminate. The above constants need to be evaluated in both regions i and ii as elaborated in Eqs. (24) and thus appropriate expressions will be derived for each region.

It is convenient to relate $\hat{A}_{11}$, $\hat{B}_{11}$, and $\hat{D}_{11}$ to known cross-sectional geometrical quantities. In particular, it can be shown that the normalized axial stiffness $\hat{A}_{11}$ is proportionally related to the composite cross-sectional area whereas $\hat{B}_{11}$ and $\hat{D}_{11}$ are the normalized first and second area moments with respect to the midsurface of the composite cross section under consideration. Thus, with the aid of Appendix B, the following expressions obtain. For the symmetric composite cross section, i.e., region ii, we get

$$\hat{A}_{11})_{ii} = \hat{A}_c/wh = \frac{1}{2}(1 + \lambda) \tag{25a}$$

$$\hat{B}_{11})_{ii} = 0 \tag{25b}$$

$$\hat{D}_{11})_{ii} = I_c/wh^3 = \frac{1}{12}\frac{1}{2}(1 + \lambda)\left[1 + 3\frac{1 - \lambda}{1 + \lambda}\frac{1}{n}\right] \tag{25c}$$

which give rise to the limiting cases:

$$n \to \infty, \qquad \lambda = 1 \tag{26a}$$

$$\hat{A}_{11})_{ii} = \frac{1}{2}(1 + \lambda), \qquad \hat{A}_{11})_{ii} = 1 \tag{26b}$$

$$\hat{B}_{11})_{ii} = 0, \qquad \hat{B}_{11})_{ii} = 0 \tag{26c}$$

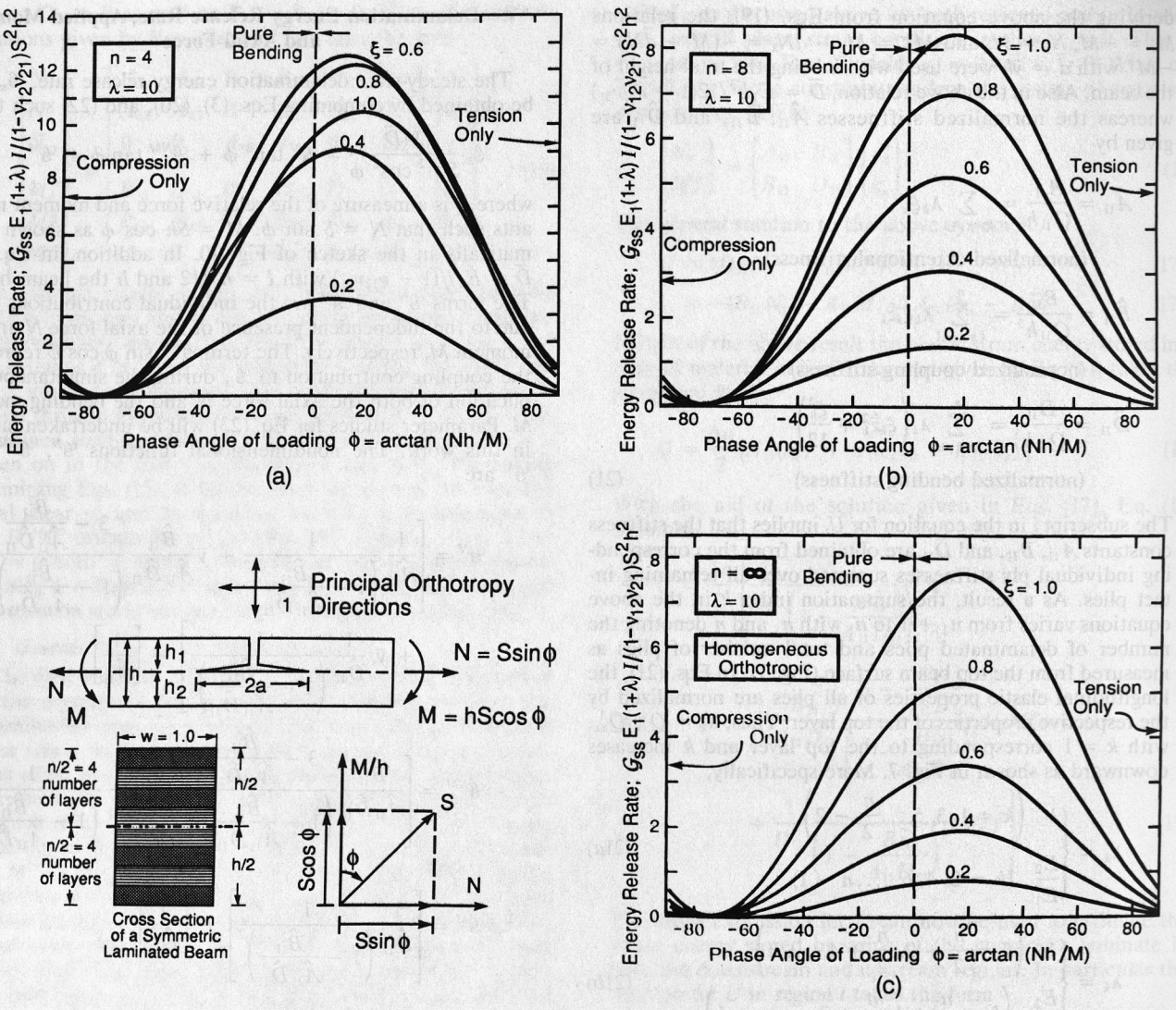

Fig. 10. Trends in the normalized steady-state delamination energy release rate $\mathcal{G}_{ss}$, with the phase angle of loading ϕ for $\lambda = 10$. In this plot, $\mathcal{G}_{ss}$ is normalized with the laminate rule of mixtures modulus, i.e., $E_1(1 + \lambda)/2$. (a), (b), and (c) correspond to different lamination morphologies wherein n, i.e., the total number of plies used, is different.

$$\hat{D}_{11})_{ii} = \frac{1}{12}\frac{1}{2}(1 + \lambda), \qquad \hat{D}_{11})_{ii} = \frac{1}{12} \tag{26d}$$

On the other hand, in region i the composite stiffnesses are

$$\hat{A}_{11})_i = A_{2c}/wh = \frac{1}{2}(1 + \lambda)\frac{1}{1 + \xi} \tag{27a}$$

$$\hat{B}_{11})_i = A_{2c}(Z_{2c} - \bar{d})/wh^2 = \frac{1}{4}(1 - \lambda)\frac{\xi}{1 + \xi}\frac{1}{n} \tag{27b}$$

$$\begin{aligned}\hat{D}_{11})_i &= [I_{2c} - A_{2c}(Z_{2c} - \bar{d})^2/wh^3] \\ &= \frac{1}{12}\frac{1}{2}(1 + \lambda)\frac{1}{(1 + \xi)^3} \\ &\quad \times \left\{(1 + \xi)^3\left[1 + 3\frac{1 - \lambda}{1 + \lambda}\frac{1}{n}\right]\right. \\ &\quad - 3\xi^2\left[1 + \frac{1 - \lambda}{1 + \lambda}\frac{1 + \xi}{n}\right]^2 \\ &\quad - 3\xi^2\left[\frac{1 - \lambda}{1 + \lambda}\frac{1 + \xi}{n}\right]^2 \\ &\quad - 3\xi(1 - \xi^2)\left[1 + 2\frac{1 - \lambda}{1 + \lambda}\frac{1}{n}\right] \\ &\quad \left. - 4\xi^3\left[1 + \frac{3}{2}\frac{1 - \lambda}{1 + \lambda}\frac{1 + \xi}{\xi}\frac{1}{n}\right]\right\}\end{aligned} \tag{27c}$$

where $\bar{d} = h_1/2$ or $\bar{d} = (h/2)\xi/(1 + \xi)$. At the limit $n \to \infty$ and $\lambda = 1$ the above equations reduce to the following simple forms

$$n \to \infty, \qquad \lambda = 1 \tag{28a}$$

$$\hat{A}_{11})_i = \frac{1}{2}(1 + \lambda)\frac{1}{1 + \xi}, \qquad \hat{A}_{11})_i = \frac{1}{1 + \xi} \tag{28b}$$

$$\hat{B}_{11})_i = 0, \qquad \hat{B}_{11})_i = 0 \tag{28c}$$

$$\hat{D}_{11})_i = \frac{1}{24}(1 + \lambda)\frac{1}{(1 + \xi)^3}, \qquad \hat{D}_{11})_i = \frac{1}{12}\frac{1}{(1 + \xi)^3} \tag{28d}$$

In Eqs. (25) through (28), λ can be obtained either via Eqs. (21*a*) and (21*b*) or from Eq. (B–2) in Appendix B. Also in the above expression, $\xi = h_1/h_2$ is the normalized notch depth and n is the total number of layers in accordance with Fig. 8.

VII. Parameter Studies

The steady-state delamination energy release rate as elaborated in Eqs. (23) to (28) is given in terms of four independent parameters, i.e., (1) the normalized notch depth $\xi = h_1/h_2$, (2) the effective longitudinal moduli ratio $\lambda = E_2/E_1$, (3) the

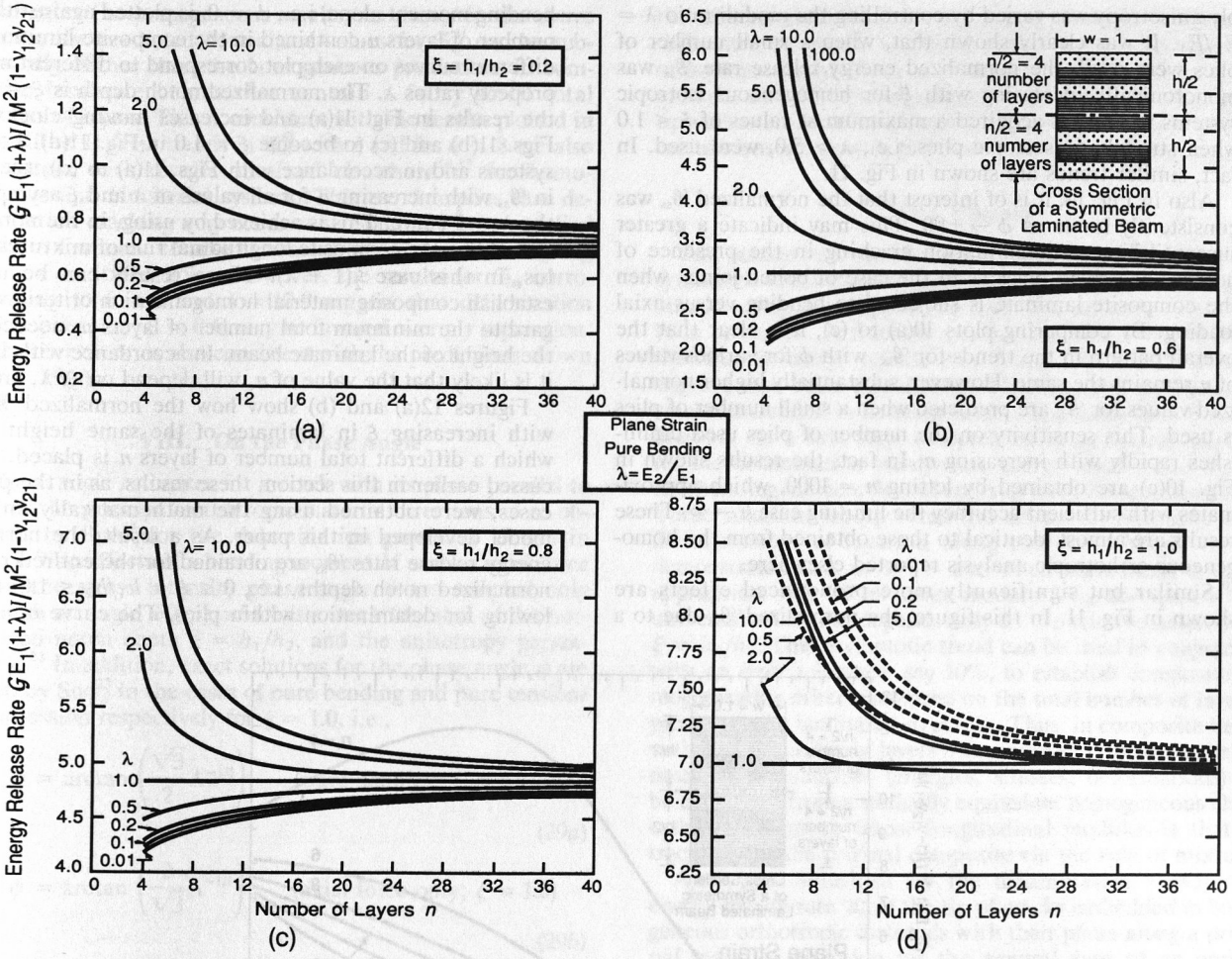

Fig. 11. Trends in the normalized steady-state delamination energy release rate $\mathcal{G}_{ss}$, with n, i.e., the total number of layers placed along the beam height. The results were obtained for a pure bending loading, i.e., $\phi = 0$. Results in figures (a), (b), (c), and (d) correspond to different normalized notch depth values.

total number of layers along the beam height n as shown in the sketch in Fig. 11(a), and (4) the phase angle of loading $\phi = \arctan(Nh/M)$. Parameter studies investigating the effects of each of the above four variables on $\mathcal{G}_{ss}$ are presented below.

Initially, the trends in normalized $\mathcal{G}_{ss}$ with respect to the phase angle of loading ϕ for varying ξ and n and constant $\lambda = 10$ are shown in Fig. 10. This type of combined loading is often encountered in the vicinity of composite fasteners where axial loads are transferred asymmetrically from one composite component to another. Different curves in each plot correspond to different values of ξ, whereas the number of layers n increases moving clockwise from plots 10(a) to (c). In obtaining the negative ϕ range results reported in the above figure, it was implicitly assumed that the notch remained open throughout the deformations process. Thus, any notch closure interference effects on the crack surface sliding are neglected in this analysis. As shown in the above plots, when the total number of plies used is larger than 8, the normalized $\mathcal{G}_{ss}$ consistently decreases with decreasing notch depth ξ throughout the described ϕ range. These trends in the normalized $\mathcal{G}_{ss}$ are consistent with those obtained for homogeneous and bimaterial systems reported elsewhere.[14,15]

On the contrary, a somewhat counterintuitive result is obtained when a small number of plies are used. As shown in Fig. 10(a), a maximum in the normalized steady-state energy release rate $\mathcal{G}_{ss}$ is predicted for $\xi = 0.6$. This is an unexpected result, but it can be explained when considering the geometrical composite morphology of the laminated beam. For example, the results shown in Fig. 10(a) correspond to a cross-ply symmetric laminated system consisting of only four plies. For $\lambda = E_2/E_1 = 10.0$, the transverse plies oriented at 90° relative to the longitudinal axis of the beam are placed on the top and bottom with the 0° plies sandwiched in the middle of the beam. For this cross-sectional morphology, delamination as signified by the separation of individual plies can only occur at any of the three interface locations present in the above system. When plies of equal thicknesses are used, as, for example, in the case depicted in Fig. 10(a), the three physically admissible delamination locations would correspond to three distinct values of $\xi = h_1/h_2$, i.e., $\xi = 1/3$, $\xi = 1$, and $\xi = 3$. In fact, the present model was initially developed assuming the discrete character of the plies with delamination occurring between plies. In order to simplify the structure of the ensuing equations, a fairly elaborate mathematical homogenization procedure was employed which resulted in the equations used to derive the results reported in this work. An added benefit of this process was that it also yielded an enhanced model capable of handling delamination occurring within individual plies. Thus, the entire range of normalized notch depths, i.e., $0 \le \xi = h_1/h_2 \le 1.0$, could be explored. It is very likely that the results reported in Fig. 10(a) obtained for $n = 4$ and $\lambda = E_2/E_1 = 10.0$ indeed represent the actual trend for the normalized $\mathcal{G}_{ss}$ with ξ. When ply separation is implied, i.e., $\xi = 1/3$ or $\xi = 1$, the predicted values for $\mathcal{G}_{ss}$ seem to be in line with the general trend of decreasing $\mathcal{G}_{ss}$ with decreasing ξ. However, when delamination is allowed to occur within the first from the top 0° ply, other competing effects primarily due to asymmetric composite coupling apparently reverse the above trend for $\mathcal{G}_{ss}$, giving rise to the results shown in Fig. (10)a. This observation was reinforced by further unpublished calculations whereby the

ply anisotropy was varied by controlling the moduli ratio $\lambda = E_2/E_1$. It was clearly shown that, when a small number of plies were used, the normalized energy release rate $\mathcal{G}_{ss}$ was monotonically increasing with ξ for homogeneous isotropic systems whereas it acquired a maximum at values of $\xi < 1.0$ when strongly anisotropic plies, i.e., $\lambda > 5.0$, were used. In fact, similar trends are shown in Fig. 11.

Also in Fig. 10, it is of interest that the normalized $\mathcal{G}_{ss}$ was consistently lower as $\phi \to \pm 90$. This may indicate a greater susceptibility to delamination cracking in the presence of notches or drilled holes as in the case of bolted joints, when the composite laminate is subjected to bending versus axial loading. By comparing plots 10(a) to (c), it is clear that the overall pattern in the trends for $\mathcal{G}_{ss}$ with ϕ for various values of n remains the same. However, substantially higher normalized values for $\mathcal{G}_{ss}$ are predicted when a small number of plies is used. This sensitivity on the number of plies used diminishes rapidly with increasing n. In fact, the results shown in Fig. 10(c) are obtained by letting $n = 1000$, which approximates with sufficient accuracy the limiting case $n \to \infty$. These results are almost identical to those obtained from the homogeneous orthotropic analysis reported elsewhere.[20] Similar but significantly more pronounced effects are shown in Fig. 11. In this figure, the normalized $\mathcal{G}_{ss}$ due to a bending moment alone, i.e., $\phi = 0$, is plotted against the total number of layers n contained in the composite laminate. The different curves on each plot correspond to different material property ratios λ. The normalized notch depth is $\xi = 0.2$ for the results in Fig. 11(a) and increases moving clockwise to Figs. 11(b) and (c) to become $\xi = 1.0$ in Fig. 11(d). For these systems and in accordance with Figs. 11(a) to (d), the trends in $\mathcal{G}_{ss}$ with increasing n for all values of λ and ξ asymptote to the $\lambda = 1$ curve. This is achieved by using, in the normalization of $\mathcal{G}_{ss}$, the composite longitudinal rule of mixtures modulus, in this case $\frac{1}{2}(1 + \lambda)$. These results can be used to establish composite material homogenization criteria with regard to the minimum total number of layers n_c needed along the height of the laminate beam. In accordance with Figs. 11, it is likely that the value of n_c will depend on ξ, λ, and ϕ.

Figures 12(a) and (b) show how the normalized $\mathcal{G}_{ss}^{M}$ vary with increasing ξ in laminates of the same height h over which a different total number of layers n is placed. As discussed earlier in this section, these results, as in the previous cases, were obtained using the mathematically enhanced model developed in this paper. As a result, the normalized energy release rates $\mathcal{G}_{ss}$ are obtained for the entired range of normalized notch depths, i.e., $0 \le \xi = h_1/h_2 \le 1.0$, thus allowing for delamination within plies. The curve $n = 40$ ap-

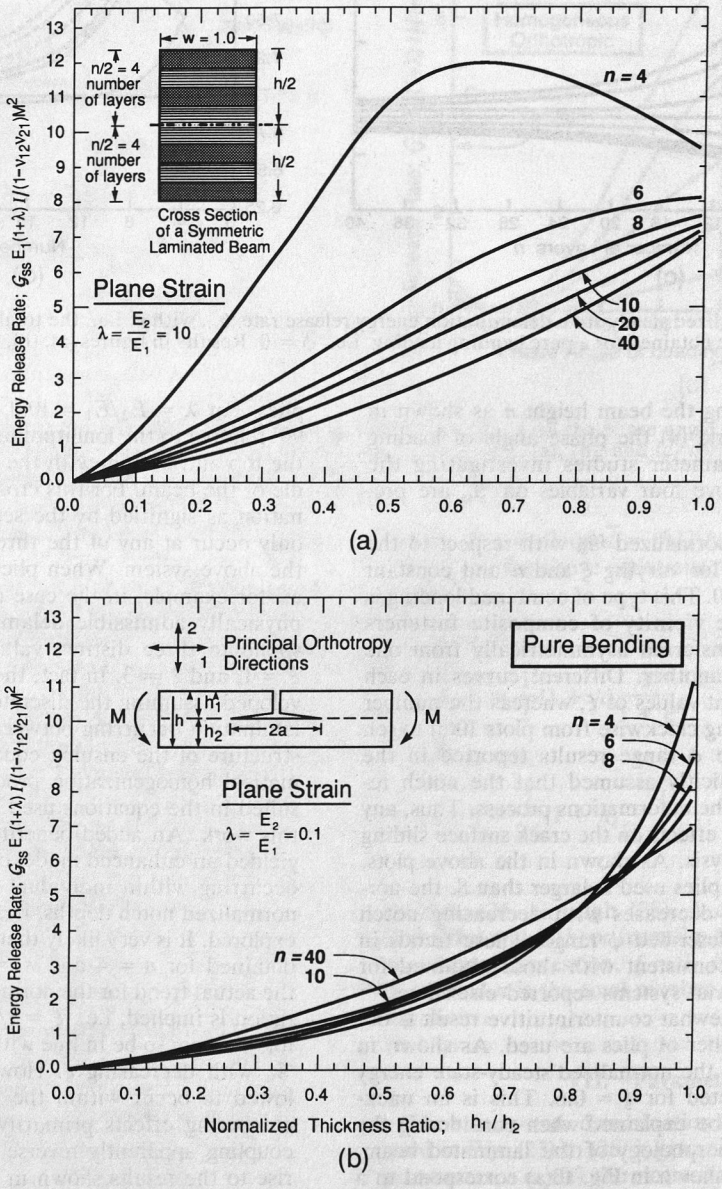

Fig. 12. Effects of notch depth h_1/h_2 on the steady-state energy release rate: (a) $\lambda = 10.0$; (b) $\lambda = 0.1$.

proximates the homogeneous results. As shown in the above figures, the predicted normalized values for $\mathcal{G}_{ss}^{M}$ can be substantially higher than the homogeneous predictions in composite laminate beams that contain a fairly small total number of layers. This is consistent with the results plotted in Figs. 10 to 11. The trends in $\mathcal{G}_{ss}^{M}$ with ξ and for $n > 8$ are also consistent with results obtained elsewhere[14,15] for homogeneous and bimaterial systems. This trend implies that delamination cracking may occur at substantially lower applied loads in laminate composites that contain comparatively big notches or drilled holes. However, the results for $\mathcal{G}_{ss}$ corresponding to $n = 4$ and $\lambda = 10.0$ suggest that delamination within plies, i.e., $\xi = 0.6$, may be favored over ply separation. This observation is also consistent with the predictions shown in Fig. 10(a).

VIII. On the Phase Angle

Phase angle estimates for a crack with its plane parallel to one of the principal orthotropic material directions were obtained by Suo[23] for the delamination geometry shown in Fig. 4. The effects of a bending moment M and an axial force N on the stress intensity phase angle ψ are coupled only through an angle $\omega(\xi,\rho)$, which is a weak function of the normalized notch depth $\xi = h_1/h_2$, and the anisotropy parameter ρ.[23] In addition, exact solutions for the phase angle ψ are given by Suo[23] in the cases of pure bending and pure tension/compression respectively for $\xi = 1.0$, i.e.,

$$\psi = \arctan\left(\frac{\sqrt{3}}{2}\Lambda^{-1/4}\right) \qquad \text{(pure bending; } \xi = 1.0\text{)} \tag{29a}$$

$$\psi = \arctan\left(\frac{2}{\sqrt{3}}\Lambda^{-1/4}\right) \qquad \text{(axial force only; } \xi = 1.0\text{)} \tag{29b}$$

where

$$\Lambda^{f} = \frac{E_2^f}{E_1^f}\,\frac{1 - (\nu_{12}^f)^2\dfrac{E_2^f}{E_1^f}}{1 - (\nu_{23}^f)^2} \tag{30a}$$

$$\Lambda^{s} = \frac{E_2^s}{E_1^s}\,\frac{1 - (\nu_{13}^s)^2}{1 - (\nu_{12}^s)^2\dfrac{E_2^s}{E_1^s}} \tag{30b}$$

with $\Lambda = \Lambda^f$ and $\Lambda = \Lambda^s$ for fiber-reinforced and symmetric cross-ply laminated composites. In the above relations, the superscripts $()^f$ and $()^s$ denote effective orthotropic quantities obtained for fiber-reinforced and laminated composite systems, respectively, as discussed elsewhere.[20] The axes 1, 2, and 3 are the principal orthotropic directions in accordance with Fig. A1. For typical composite systems, the values of ψ predicted via Eq. (29*a*) and (29*b*) are of the order of 40° to 50°, indicative of the mixed-mode nature of delamination cracking under either a pure bending or axial loading. These phase angles in conjunction with the energy release rates derived earlier (see Eqs. (23) and (24)) fully characterize stress and displacement fields around crack tips of cracks embedded in principal orthotropic direction in homogeneous orthotropic ideally brittle materials. In particular, $\mathcal{G}_{ss}$ and ψ would dominate the stress and strain fields in region *ii* shown in Fig. 3(a) as discussed earlier in this work. Therefore, delamination cracking in these systems can be understood in terms of ψ and $\mathcal{G}_{ss}$. However, the results regarding the phase angle reported above should be used with greater caution when cracking occurs in either a fiber-reinforced or a laminated composite. In either of these systems and whenever failure occurs at a scale much smaller than the fiber radius of the layer thickness, concepts from bimaterial fracture may be necessary for the characterization of such cracking process. Despite this difficulty, the phase angles obtained from a homogeneous orthotropic analysis can be used as remote quantities which, as in the case of the sandwich geometry,[24] can be linked to the tip values via local mechanics. More rigorous finite-element calculations are now in progress in addressing these issues.

IX. Closure

The steady-state mechanics of delamination cracking in symmetric laminated prenotched beams, subjected to a combined loading of an applied moment and an axial force, have been presented. A fracture meachanics framework based on the near-tip energy release rate $\mathcal{G}$ and the associated phase angle ψ has been established. The near-tip mechanics of cracks embedded in heterogeneous composites have been addressed. As a first step, comprehensive analytical solutions for the delamination steady-state energy release rate $\mathcal{G}_{ss}$ due to a bending moment M and an axial force N were developed. These solutions incorporated the effects of arbitrarily small finite number of layers n along the beam height. It was demonstrated that as $n \to \infty$ and when normalized with the appropriate rule of mixtures modulus, $\mathcal{G}_{ss}$ asymptotes to a universal value that depends only on the relative notch depth $\xi = h_1/h_2$. This asymptotic trend can be used in conjunction with an *error* tolerance, say 10%, to establish composite homogenization criteria imposed on the total number of layers n present in the laminated structure. Thus, in composite beams with a total number of layers n exceeding a critical number n_c, mechanical quantities (energies, stresses, deformations) can be calculated from a statically equivalent homogeneous elastic orthotropic system whose longitudinal modulus is that extracted from the original composite via the rule of mixtures.

Analytical solutions for the delamination steady-state energy release rate $\mathcal{G}_{ss}$ at the tip of cracks embedded in homogeneous orthotropic materials with their plane along a principal material direction for the general case of an applied moment and an axial force were also obtained at the limit $n \to \infty$. The associated phase angle ψ due to the independent application of the moment M or the axial force N was found to be of the order of 40° to 50°, indicative of the mixed-mode nature of delamination cracking under either a pure bending or axial loading.

Interlaminar shear effects on the near-tip mechanics have been neglected. In addition, the analysis does not account for possible nonlinear failure processes in the region close to the crack tip, for example, fibers bridging the main crack, which may potentially shield the crack tip from the applied loads. In composites with such operating mechanisms and under the assumption of a small scale process zone, apparent fracture toughnesses for delamination cracking can be obtained using the results for $\mathcal{G}_{ss}$ derived in this study. Thus, as a major benefit of this work, the results of this analysis can be used in conjunction with experimental data to establish critical delamination energies and crack resistance curves for fiber-reinforced/laminated composite systems. The analysis is particularly suitable for design specifications based on toughness of laminated composites and composite fasteners such as bolted joints.

APPENDIX A

Some Relevant Mechanics

(1) Constitutive Relations of an Orthotropic Medium

The inverse generalized Hooke's law for a linear elastic generally anisotropic material can be written using indicial notation as follows:[23,25–27]

$$\varepsilon_i = S_{ij}\sigma_j \qquad (i, j = 1 \text{ to } 6) \tag{A–1}$$

In Eq. (A–1) summation over the repeated index j is implied

from 1 to 6. The matrix $[S_{ij}]$ is a full 6×6 symmetric matrix containing the anisotropic material compliances. For an orthotropic material oriented along its principal axis as shown in Fig. A1(a), uncoupling between tension and shear is obtained and the strain–stress relations take the matrix form

$$\begin{Bmatrix} \varepsilon_x \\ \varepsilon_y \\ \varepsilon_z \\ \gamma_{yz} \\ \gamma_{zx} \\ \gamma_{xy} \end{Bmatrix} = \begin{bmatrix} \frac{1}{E_1} & \frac{-\nu_{12}}{E_1} & \frac{-\nu_{13}}{E_1} & 0 & 0 & 0 \\ \frac{-\nu_{21}}{E_2} & \frac{1}{E_2} & \frac{-\nu_{23}}{E_2} & 0 & 0 & 0 \\ \frac{-\nu_{31}}{E_3} & \frac{-\nu_{32}}{E_3} & \frac{1}{E_3} & 0 & 0 & 0 \\ 0 & 0 & 0 & \frac{1}{G_{23}} & 0 & 0 \\ 0 & 0 & 0 & 0 & \frac{1}{G_{31}} & 0 \\ 0 & 0 & 0 & 0 & 0 & \frac{1}{G_{12}} \end{bmatrix} \begin{Bmatrix} \sigma_x \\ \sigma_y \\ \sigma_z \\ \tau_{yz} \\ \tau_{zx} \\ \tau_{xy} \end{Bmatrix} \tag{A–2}$$

In accordance with Fig. A1(a), E_i, $i = 1, 3$, are the elastic moduli in the principal 1, 2, and 3 directions, respectively; G_{23}, G_{31}, and G_{12} are the shear moduli in the 2–3, 3–1, and 1–2 planes, respectively. The Poisson's ratios ν_{12}, ν_{13}, and ν_{23} are defined such that $\nu_{ij} = -\varepsilon_i/\varepsilon_j$ due to an applied normal stress σ_i. It follows from constitutive symmetry that $\nu_{ij}/E_i = \nu_{ji}/E_j$ for all permissible ij pairs. A reduced form for the constitutive relations obtains for systems in either plane stress or plane strain.[23,25] In laminated theories,[21,22] individual uniaxially fiber-reinforced plies are treated as orthotropic systems subjected to *plane stress* conditions. Overall, plane stress or plane strain conditions are imposed via a wide or narrow "beam" consideration for the structural laminate as elaborated elsewhere in this article. Thus, the constitutive relations for a ply in plane stress oriented along its principal axis reduce to [21,22]

$$\varepsilon_i = b_{ij}\sigma_j \qquad (i, j = 1, 2, 6) \tag{A–3}$$

and in matrix notation take the form

$$\begin{Bmatrix} \varepsilon_x \\ \varepsilon_y \\ \gamma_{xy} \end{Bmatrix} = \begin{bmatrix} \frac{1}{E_1} & \frac{-\nu_{12}}{E_1} & 0 \\ \frac{-\nu_{21}}{E_2} & \frac{1}{E_2} & 0 \\ 0 & 0 & \frac{1}{G_{12}} \end{bmatrix} \begin{Bmatrix} \sigma_x \\ \sigma_y \\ \tau_{xy} \end{Bmatrix} \tag{A–4}$$

where $[b]$ is now the reduced compliance matrix and its elements b_{ij} are obtained from a direct comparison between Eqs. (A–3) and (A–4). By inverting Eqs. (A–3) and (A–4), the stresses can be expressed in terms of the strains via the reduced stiffness matrix $[Q]$, i.e.,

$$\sigma_i = Q_{ij}\varepsilon_j \qquad (i, j = 1, 2, 6) \tag{A–5}$$

which equations are written in a matrix form as follows:

$$\begin{Bmatrix} \sigma_x \\ \sigma_y \\ \tau_{xy} \end{Bmatrix} = \begin{bmatrix} \frac{E_1}{1 - \nu_{12}\nu_{21}} & \frac{\nu_{12}E_2}{1 - \nu_{12}\nu_{21}} & 0 \\ \frac{\nu_{21}E_1}{1 - \nu_{12}\nu_{21}} & \frac{E_2}{1 - \nu_{12}\nu_{21}} & 0 \\ 0 & 0 & G_{12} \end{bmatrix} \begin{Bmatrix} \varepsilon_x \\ \varepsilon_y \\ \gamma_{xy} \end{Bmatrix} \tag{A–6}$$

If a misalignment exists between the principal orthotropic directions and the reference axis (see Fig. A1(c)), the reduced stiffness matrix becomes a full 3×3 matrix as follows:

$$\sigma_i = \bar{Q}_{ij}\varepsilon_j \qquad (i, j = 1, 2, 6) \tag{A–7}$$

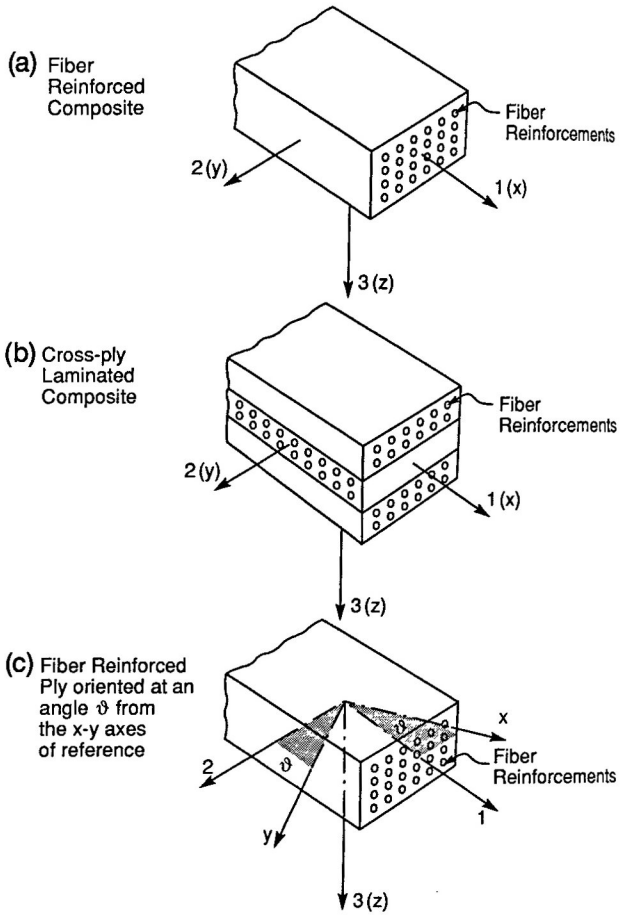

Fig. A1. Principal orthotropic directions in a homogenized composite: (a) a fiber-reinforced ply, (b) a cross-ply laminate, (c) an ortotropic ply oriented at an angle θ with respect to the reference axes x, y.

The matrix form of Eq. (A–7) is

$$\begin{Bmatrix} \sigma_x \\ \sigma_y \\ \tau_{xy} \end{Bmatrix} = \begin{bmatrix} \bar{Q}_{11} & \bar{Q}_{12} & \bar{Q}_{16} \\ \bar{Q}_{12} & \bar{Q}_{22} & \bar{Q}_{26} \\ \bar{Q}_{16} & \bar{Q}_{26} & \bar{Q}_{66} \end{bmatrix} \begin{Bmatrix} \varepsilon_x \\ \varepsilon_y \\ \gamma_{xy} \end{Bmatrix} \tag{A–8}$$

with

$$\bar{Q}_{11} = Q_{11}\cos^4\theta + Q_{22}\sin^4\theta + 2(Q_{12} + 2Q_{66})\sin^2\theta\cos^2\theta \tag{A–9a}$$

$$\bar{Q}_{22} = Q_{11}\sin^4\theta + Q_{22}\cos^4\theta + 2(Q_{12} + 2Q_{66})\sin^2\theta\cos^2\theta \tag{A–9b}$$

$$\bar{Q}_{66} = (Q_{11} + Q_{22} - 2Q_{12} - 2Q_{66})\sin^2\theta\cos^2\theta + Q_{66}(\sin^4\theta + \cos^4\theta) \tag{A–9c}$$

$$\bar{Q}_{12} = (Q_{11} + Q_{22} - 4Q_{66})\sin^2\theta\cos^2\theta + Q_{12}(\sin^4\theta + \cos^4\theta) \tag{A–9d}$$

$$\bar{Q}_{16} = (Q_{11} - Q_{12} - 2Q_{66})\sin\theta\cos^3\theta - (Q_{22} - Q_{12} - 2Q_{66})\sin^3\theta\cos\theta \tag{A–9e}$$

$$\bar{Q}_{26} = (Q_{11} - Q_{12} - 2Q_{66})\sin^3\theta\cos\theta - (Q_{22} - Q_{12} - 2Q_{66})\sin\theta\cos^3\theta \tag{A–9f}$$

where θ is the angle of rotation between the principal orthotropic ply directions 1 and 2 and the x, y axes of reference as shown in Fig. A1(c).

In the case of an orthotropic material where the x and y and 1 and 2 axes are aligned, there are only four nonzero independent elastic constants, i.e., b_{11}, $b_{12} = b_{21}$, b_{22} and b_{66} with

$b_{16} = b_{26} = 0$, as summarized via Eqs. (A–3) and (A–4). In addition, Suo[23] demonstrated that the solution to the traction boundary value problem within a simply connected domain depends only on two nondimensional elastic parameters, i.e.,

$$\Lambda = \frac{b_{11}}{b_{22}}, \qquad \rho = \frac{2b_{12} + b_{66}}{2\sqrt{b_{11}b_{22}}} \tag{A–10}$$

When $\Lambda = 1$ the material anisotropy reduces to cubic symmetry and when $\Lambda = \rho = 1$ the material becomes transversely isotropic. As discussed by Suo,[23] a positive definite strain energy density is obtained for $\Lambda > 0$ and $-1 < \rho < \infty$.

(2) Near-Tip Mechanics in an Orthotropic Material

When the composites are uniaxially reinforced, such that the anisotropic elastic properties are spatially homogeneous, the crack tip fields have the conventional square root singularity and are then characterized by the stress intensity factor, K, in mode I and mode II such that the stresses at a distance r ahead of the crack tip are given asymptotically by

$$\sigma_y + i\sigma_{xy} = \frac{K_I + iK_{II}}{\sqrt{2\pi r}} \tag{A–11}$$

It is often convenient to express the stress intensities in a complex form such that

$$K = K_I + iK_{II} = |K|e^{i\psi} \tag{A–12}$$

where $i = \sqrt{-1}$, $|K|$ is the modulus of the stress intensity factor and ψ is its phase angle. It is clear from Eq. (A–11) that the units of K are the same as in the case of cracks in homogeneous materials and unlike the bimaterial case, its phase angle ψ is scale insensitive. In addition, the relative opening and sliding of the crack surfaces at a distance r behind the crack tip for a crack in a principal direction of an orthotropic body are given by

$$\Delta u_y + i\Delta u_x = 8b_{11}q[\Lambda^{-3/4}K_I + i\Lambda^{-1/4}K_{II}]\sqrt{\frac{r}{2\pi}} \tag{A–13}$$

where $q = \sqrt{(1 + \rho)/2}$ and b_{11} and Λ as before. The energy release rate is related to the stress intensity factors by[23,28]

$$\mathcal{G} = b_{11}n[\Lambda^{-3/4}K_I^2 + i\Lambda^{-1/4}K_{II}^2] \tag{A–14}$$

Therefore, the task of understanding the mechanics at tips of cracks positioned in the principal direction of an orthotropic material reduces to one wherein only $|K|$ and ψ or $\mathcal{G}$ and ψ are to be determined. These quantities are, by and large, load and geometry dependent.

APPENDIX B

Cross-Sectional Quantities of Composite Laminates

In this appendix the special case of the delaminated symmetric beam shown in Fig. 8(a) is considered. This geometric morphology represents a typical 0°/90° symmetric laminate fiber-reinforced composite. In such a case, the longitudinal and transverse moduli and Poisson's ratios for each ply are E_1, ν_{12} and E_2, ν_{21}, respectively. The thickness of each layer is t, and the total number of layers is $n = 2m$ with m being the number of layers in the symmetric half of the laminate composite. Also as shown in Fig. 8(a) the notch depth is h_1 and thus the delamination crack lies at the interface of the n_1 and $n_1 + 1$ layers from the top. The necessary geometric quantities are now derived using the cross-sectional sketched in Fig. 8(b). Let A_c, A_{1c}, A_{2c} be the composite areas of the uncracked beam, the section above, and the section below the delamination crack, respectively. Then

$$A_c = 2w\sum_{i=1}^{m}\lambda_i t_i = 2wt\sum_{i=1}^{m}\lambda_i = \frac{1}{2}(1 + \lambda)wh \tag{B–1}$$

where $t/h = 1/n = 1/2m$ has been used. Transformation of individual ply areas is performed with respect to the orientation of the top ply and thus the moduli ratio λ for the ith layer takes the form

$$\lambda_i = \begin{cases} \lambda = \dfrac{E_2}{E_1} & (i = 1, 3, 5, \ldots, m - 1) \\ 1 & (i = 2, 4, 6, \ldots, m) \end{cases} \tag{B–2}$$

where m is now measured from the laminate midsurface as shown in Fig. 8. Similarly

$$A_{1c} = w\sum_{i=n_1+1}^{m}\lambda_i t_i = \frac{1}{2}(1 + \lambda)\frac{\xi}{1 + \xi}wh \tag{B–3a}$$

$$A_{2c} = A_c - A_{1c} = \frac{1}{2}(1 + \lambda)\frac{1}{1 + \xi}wh \tag{B–3b}$$

where $\xi = h_1/h_2$ now denotes the normalized notch depth. The distance of the neutral axis of the composite areas A_{1c} and A_{2c} from the symmetry plane of the uncracked section which in Fig. 8b are denoted by Z_{1c} and Z_{2c} are given by

$$Z_{1c} = \frac{S_y^1}{A_{1c}} = \sum_{i=n_1+1}^{m}\lambda_i t_i z_s^i \Big/ \sum_{i=n_1+1}^{m}\lambda_i t_i = -\frac{h}{2}\frac{1}{1 + \xi}\left[1 + \frac{1 - \lambda}{1 + \lambda}\frac{1 + \xi}{n}\right] \tag{B–4a}$$

$$Z_{2c} = \frac{S_y^2}{A_{2c}} = A_c - A_{1c}Z_{1c} = +\frac{h}{2}\frac{\xi}{1 + \xi}\left[1 + \frac{1 - \lambda}{1 + \lambda}\frac{1 + \xi}{n}\right] \tag{B–4b}$$

where S_y^1 and S_y^2 are the first moments of the composite areas A_{1c} and A_{2c} with respect to the y axis shown in Fig. 8(a). Also in the above relation, z_s^i denotes the distance of ply i from the midsurface of the uncracked section such that $z_s^i = (n - n_1)t + (2i - 1)t/2$. Then the composite principal second moments of inertia I_c, I_{1c}, and I_{2c} are given by

$$I_c = 2\sum_{i=1}^{m}\lambda_i\frac{wt^3}{12} + 2\sum_{i=1}^{m}\lambda_i wt\left((2i - 1)\frac{t}{2}\right)^2 = \frac{wh^3}{12}\frac{1}{2}(1 + \lambda)\left[1 + 3\frac{1 - \lambda}{1 + \lambda}\frac{1}{n}\right] \tag{B–5}$$

$$I_{1c} = \sum_{i=1}^{n_1}\lambda_i\frac{wt^3}{12} + \sum_{i=1}^{n_1}\lambda_i wt\,(z_s^i - Z_{1c})^2 \tag{B–6}$$

where z_s^i is as above. Rewriting Eq. (B–6), we get

$$I_{1c} = \frac{wh^3}{12}\frac{1}{2}(1 + \lambda)\left(\frac{\xi}{1 + \xi}\right)^3 \times \left\{-\frac{3}{\xi^2}\left[1 + \frac{1 - \lambda}{1 + \lambda}\frac{1 + \xi}{n}\right]^2 + \frac{3(1 - \xi^2)}{\xi^2}\left[1 + 2\frac{1 - \lambda}{1 + \lambda}\frac{1}{n}\right] + 4\left[1 + \frac{3}{2}\frac{1 - \lambda}{1 + \lambda}\frac{1 + \xi}{\xi}\frac{1}{n}\right]\right\} \tag{B–7}$$

Also

$$I_{2c} = I_c - \{I_{1c} + A_{1c}Z_{1c}^2 + A_{2c}Z_{2c}^2\} \tag{B–8}$$

or

$$I_{2c} = \frac{wh^3}{12}\frac{1}{2}(1+\lambda)\frac{1}{(1+\xi)^3} \times \left\{(1+\xi)^3\left[1+3\frac{1-\lambda}{1+\lambda}\frac{1}{n}\right] - 3\xi^2\left[1+\frac{1-\lambda}{1+\lambda}\frac{1+\xi}{n}\right]^2 - 3\xi(1-\xi^2)\left[1+2\frac{1-\lambda}{1+\lambda}\frac{1}{n}\right] - 4\xi^3\left[1+\frac{3}{2}\frac{1-\lambda}{1+\lambda}\frac{1+\xi}{\xi}\frac{1}{n}\right]\right\} \quad \text{(B-9)}$$

Some Limiting Cases:

(1) As expected when $\lambda = 1$ (homogeneous system)

$$I_c = \frac{wh^3}{12} \quad \text{(B-9}a\text{)}$$

$$I_{1c} = \frac{wh^3}{12}\left(\frac{\xi}{1+\xi}\right)^3 \quad \text{(B-9}b\text{)}$$

$$I_{2c} = \frac{wh^3}{12}\frac{1}{(1+\xi)^3} \quad \text{(B-9}c\text{)}$$

(2) At the limit $n \to \infty$

$$I_c = \frac{wh}{12}\frac{1}{2}(1+\lambda) \quad \text{(B-10}a\text{)}$$

$$I_{1c} = \frac{wh^3}{12}\frac{1}{2}(1+\lambda)\left(\frac{\xi}{1+\xi}\right)^3 \quad \text{(B-10}b\text{)}$$

$$I_{2c} = \frac{wh^3}{12}\frac{1}{2}(1+\lambda)\frac{1}{(1+\xi)^3} \quad \text{(B-10}c\text{)}$$

Acknowledgments: I am indebted to Professors Anthony G. Evans at UCSB/Materials Department and the late Harold W. Lord at MTU/ME-EM Department for many helpful discussions and their constant encouragement during the course of this work.

References

[1]A. G. Evans, "The Mechanical Performance of Fiber-Reinforced Ceramic Matrix Composites," *Mater. Sci. Eng.*, **A107**, 227–39 (1989).

[2]O. Sbaizero and A. G. Evans, "Tensile and Shear Properties of Laminated Ceramic Matrix Composites," *J. Am. Ceram. Soc.*, **69**, 481–86 (1986).

[3]K. M. Prewo, "Tension and Flexural Strength of Silicon Carbide Fibre-Reinforced Glass Ceramics," *J. Mater. Sci.*, **21**, 3590–600 (1986).

[4]O. Sbaizero, P. G. Charalambides, and A. G. Evans, "Delamination Cracking in a Laminated Ceramic Matrix Composite," *J. Am. Ceram. Soc.*, **73** [7] 1936–40 (1990).

[5]B. Dalgleish and A. G. Evans, "Delamination Cracking in a Fiber Reinforced Ceramic Matrix Composite"; unpublished work.

[6]S. S. Wang, "Composite Materials; Testing and Design," *ASTM Spec. Tech. Publ.*, 642–63 (1979).

[7]M. F. Ashby, E. E. Easterling, R. Harrysson, and S. K. Maiter, "The Fracture and Toughness of Wood," *Proc. R. Soc. London*, **A398**, 261–80 (1985).

[8]P. G. Charalambides and A. G. Evans, "Debonding Properties in Residually Stressed Brittle Matrix Composites," *J. Am. Ceram. Soc.*, **72** [5] 746–53 (1989).

[9]M. D. Thouless and A. G. Evans, "Effects of Pull-Out on the Mechanical Properties of Ceramic Matrix Composites," *Acta Metall.*, **36** [3] 517–22 (1988).

[10]L. S. Sigl and A. G. Evans, "Effects of Residual Stress and Frictional Sliding on Cracking and Pull-Out in Brittle Matrix Composites," *Mech. Mater.*, **8**, 1–12 (1989).

[11]J. R. Rice, "Mathematical Analysis in the Mechanics of Fracture"; pp. 192–308 in *Fracture, An Advance Treatise*, Vol. 2. Edited by H. Liebowitz. Academic Press, New York, 1968.

[12]J. R. Rice, "Elastic Fracture Mechanics Concepts for Interfacial Cracks," *J. Appl. Mech.*, **55**, 98–103 (1988).

[13]J. W. Hutchinson, M. E. Mear, and J. R. Rice, "Crack Paralleling an Interface Between Dissimilar Materials," *J. Appl. Mech.*, **54**, 828–32 (1987).

[14]P. G. Charalambides, J. Lund, A. G. Evans, and R. M. McMeeking, "A Test Specimen for Determining the Fracture Resistance of Bimaterial Interfaces," *J. Appl. Mech.*, **56**, 77–82 (1989).

[15]P. G. Charalambides, H. C. Cao, J. Lund, and A. G. Evans, "Development of a Test Method in Measuring the Mixed Mode Fracture Resistance of Bimaterial Interfaces," *Mech. Mater.*, **8**, 269–83 (1990).

[16]H. C. Cao and A. G. Evans, "An Experimental Study of the Fracture Resistance of Bimaterial Interfaces," *Mech. Mater.*, **7**, 295–305 (1989).

[17]A. G. Evans and J. W. Hutchinson, "Effects of Non-Planarity on the Mixed Mode Fracture Resistance of Bimaterial Interfaces," *Acta Metall.*, **37** [3] 909–16 (1989).

[18]M. Comninou and D. Schmueser, "The Interface Crack in a Combined Tension-Compression and Shear Field," *J. Appl. Mech.*, **46**, 345–48 (1979).

[19]N. Aravas and S. M. Sharma, "An Elastoplastic Analysis of the Interface Crack with Contact Zones"; unpublished work.

[20]P. G. Charalambides, "Steady-State Delamination Cracking in Fiber Reinforced Brittle Matrix Composites"; unpublished work.

[21]S. W. Tsai, T. N. Massard, and I. Susuki, *Composites Design*, 3rd ed. Think Composites, Dayton, OH, 1987.

[22]J. T. Oden and E. A. Ripperger, *Mechanics of Elastic Structures*, 2nd ed. Hemisphere Publishing Corp., Washington, 1980.

[23]Z. Suo, "Delamination Specimens for Orthotropic Materials," *J. Appl. Mech.*, **57**, 627–34 (1990).

[24]Z. Suo and J. W. Hutchinson, "On Sandwich Test Specimen for Measuring Interface Crack Toughness," *Mater. Sci. Eng.*, **A107**, 135–43 (1989).

[25]Z. S. G. Lekhnitskii, *Theory of an Anisotropic Body*. Edited by J. J. Brandstatter. Holden–Day, San Francisco, CA, 1963.

[26]G. C. Sih, P. C. Paris, and G. R. Irwin, "On Cracks in Rectilinearly Anisotropic Bodies," *Int. J. Fract.*, **1**, 189–203 (1965).

[27]D. Hull, *An Introduction to Composite Material*. Cambridge University Press, Cambridge, U.K., 1981.

[28]R. M. Christensen, *Mechanics of Composite Materials*. Wiley, New York, 1979. □